https://doi.org/10.5194/egusphere-2026-5522
Preprint. Discussion started: 27 October 2026
© Author(s) 2026. CC BY 4.0 License.

CryoSwath: a CryoSat-2 swath processor and monthly surface elevation dataset for Arctic mountain glaciers

Jan Haacker[1,2] and Bert Wouters[1]

[1]Delft University of Technology, Delft, The Netherlands
[2]University of Natural Resources and Life Sciences (BOKU), Vienna, Austria

Correspondence: Jan Haacker (jan.haacker@boku.ac.at) and Bert Wouters (bert.wouters@tudelft.nl)

Abstract. Mountain glaciers are projected to lose between 26 and 41 % of their mass from 2015 until 2100 depending on the assumed global temperature change scenario. Melting glacier ice contributes to sea-level rise and reduces terrestrial freshwater storage. Monitoring glacier change contributes to the evidence base that can help affected communities assess whether adaptation is necessary and identify appropriate measures. We introduce the open-source Python package CryoSwath, which estimates glacier surface elevations from freely available CryoSat-2 altimetry data. Alongside, we establish a process-informed interpolation method and estimate uncertainty correlations from systematic comparison to a photogrammetry-based reference (ArcticDEM strips). Further, we present a CryoSwath-produced dataset of monthly sampled, three-month rolling-window glacier surface elevation estimates at a 500 m resolution covering nearly all glaciated areas in the Arctic during the period 2010 to 2024. We find that glaciers in Alaska are thinning most rapidly while those in Arctic Canada North and Greenland Periphery show the slowest region-wide change rates. However, negative trends are ubiquitous with an Arctic-wide mass loss of 197 ± 10 Gt yr^{-1}.

The dataset opens research opportunities to study these changes in detail and to contextualize the glacier response to variability in atmospheric or oceanic forcing. The open software enables non-expert researchers from different fields to efficiently process CryoSat-2 data at scale over glaciated regions and inspect the data at intermediate processing stages. The user has full control over the processing and, with that, the means to derive and output non-default quantities.

1 Introduction

In our rapidly changing climate, together with other Earth system components, the cryosphere constantly adapts. Mountain glaciers in particular are a visible example of how global warming affects our planet, as they react over timescales of a few years to decades to increasing temperatures. The shrinking and retreat of these freshwater reservoirs not only affect global sea level but also have profound effects on local freshwater availability, ecosystems, and economic activities, and may trigger hazards like flooding and landslides. Monitoring glaciers to improve our understanding of their current and future behavior is, thus, both of great scientific and societal interest. Rounce et al. (2023) project glacier mass losses of 26 to 41 % between 2015 and 2100 for global warming scenarios of 1.5 to 4 °C relative to preindustrial levels.

https://doi.org/10.5194/egusphere-2026-5522
Preprint. Discussion started: 27 October 2026
© Author(s) 2026. CC BY 4.0 License.

In-situ measurements of glacier mass balance provide invaluable information on the state of mountain glaciers, yet can only cover a small fraction of the approximately 270,000 glaciers on our planet. Remote sensing provides a platform to map glaciers on a global scale and has accelerated our understanding of how glaciers respond to changes in atmospheric and oceanic forcing (Gardner et al., 2013; Wouters et al., 2019; Ciracì et al., 2020; Berthier et al., 2023; Dussaillant et al., 2025; The GlaMBIE Team et al., 2025).

Satellite gravimetry by the GRACE and GRACE-FO missions measures mass changes directly at monthly resolution. However, the horizontal resolution is on the order of 100 kilometers, too coarse to resolve individual glaciers and separate smaller mountain glaciers from other sources of mass variations in their surroundings, e.g., due to hydrological processes.

An indirect way of assessing glacier mass balance is by considering their change in elevation. Digital elevation models (DEMs) of glaciers based on either optical stereo-photogrammetry or bistatic InSAR obtained at different moments in time can be differenced to obtain elevation change estimates. The resulting datasets are typically of high spatial resolution [$\mathcal{O}$(1–10 m)] but lower temporal resolution. The latter is, partly, because of a lack of dedicated missions for this purpose, but also due to, e.g., the dependence on clear-sky and daylight conditions for optical imagery, and penetration of the radar signal into the snow and firn layer for InSAR, which requires that, ideally, DEMs from approximately the same time of the year are differenced to reduce biases related to changes in the penetration depth (see Berthier et al. (2023) for a detailed discussion). The elevation changes obtained through geodetic methods like DEM-differencing require assumptions about the density of the observed volume changes to be translated to mass balance estimates, a non-trivial step that introduces major uncertainties (Huss, 2013).

Another way of estimating glacier elevation changes is through repeat satellite altimetry. ICESat, the first laser altimetry mission dedicated to cryosphere applications, was launched in 2003, followed by ICESat-2 in 2018. Altimetry does not depend on daylight conditions, but when using laser, it still depends on clear-sky conditions. A main advantage of laser altimetry is the high precision and accuracy of surface elevation measurements for a given, small footprint, on the order of 10 m in the case of ICESat-2. The small footprint, however, leads to a sparser spatiotemporal coverage compared to radar altimetry.

While the footprint and accuracy of early radar missions was insufficient to study mountain glaciers, this changed with the launch of the first SARIn (see below) altimeter, CryoSat-2, the European Space Agency's (ESA) mission dedicated to measuring surface elevation changes in the cryosphere (Wingham et al., 2006). The original mission design targeted sea ice and large ice sheets (Drinkwater et al., 2004). This mission, for the first time, also measured the angle of arrival of the echo in the so-called SARIn mode, using a second antenna that is mounted perpendicular to the direction of flight, allowing to precisely geolocate the echo point in sloping terrain.

Traditionally, radar altimetry retracks the recorded signal echo to derive the range to the point of closest approach (POCA), using the first increase and peak of the power of the echo waveform. Hawley et al. (2009) suggested exploiting the full recording of the return signal may increase the number of across-track elevation measurements by an order of magnitude. Gray et al. (2013) proved the concept—which became known as "swath processing"—and its applicability to CryoSat-2 data and mountain glaciers. Today, there is a large body of studies that rely on CryoSat-2 swath elevation estimates (Foresta et al., 2016, 2018; Jakob et al., 2021; Jakob and Gourmelen, 2023). ESA provides public point and gridded elevation products through CryoTEMPO-EOLIS, including uncertainty estimates. The Baseline 3 point-product variables listed in its handbook (Issue 4.1)

https://doi.org/10.5194/egusphere-2026-5522
Preprint. Discussion started: 27 October 2026
© Author(s) 2026. CC BY 4.0 License.

do not include waveform power or coherence (CryoTEMPO-EOLIS, 2026). Access to these products does not provide control over the processing choices used to derive them. Furthermore, the standard workflow applied to the CryoSat-2 waveforms to derive surface elevations may not always align with the needs of the end user, when they want to perform advanced analyses.

Here, we introduce CryoSwath, a free and open-source Python package that processes ESA's freely available CryoSat-2 SARIn L1b waveform data and produces glacier surface elevation estimates. Designed to enable non-expert radar altimetry data users to swath process CryoSat-2 data, CryoSwath provides both pipelines using predefined default parameters and full control over processing the data at all stages. Alongside, we publish monthly sampled, three-month rolling-window surface elevation data in a 500 m square grid for the mountain glaciers and ice caps of the Arctic derived by CryoSwath 0.2.2 and time series of average surface elevation changes.

2 Initial data

In this section, we introduce the datasets that we build on. These are ESA's CryoSat-2 SARIn L1b product at baseline E (European Space Agency, 2019), the digital elevation model (DEM) ArcticDEM at version 4.1 (Porter et al., 2023), and glacier outlines and other data of the Randolph Glacier Inventory (RGI) at version 7.0 (RGI 7.0 Consortium, 2023).

2.1 ESA's SARIn L1b product

As a Ku-band radar altimeter, CryoSat-2 transmits a radar pulse and receives part of the signal that is reflected by matter at or below the surface, termed "scatterers". For glacier settings, this means that the back-scattered signal will typically be a combination of reflections from the surface, and reflections from the snow volume, caused by density variations within the snowpack. The interested reader may refer to Morris et al. (2022) to learn about the relation between seasons and the scatterer location relative to the surface. Based on the travel time, the distance to the echo location can be estimated. CryoSat-2 operates in three different modes: a low-resolution mode, a Synthetic Aperture Radar (SAR) mode, and a SAR Interferometric (SARIn) mode. SAR uses multiple coherently transmitted signals to synthesize an effectively larger antenna along the satellite's flight path (Raney, 1998). The interferometric measurements require a second antenna, mounted perpendicular to the travel direction. Comparing the recordings of both yields a phase difference that allows us to determine the across-track direction to the origin of the reflected signal. SARIn mode is active over glaciers and, further, is a prerequisite for swath processing since only SARIn delivers the critical phase difference information. SARIn acquisition is governed by ESA's geographic mode mask, so glacier coverage is limited to areas observed in this mode (European Space Agency, 2023).

In SARIn mode, CryoSat-2 sends and receives about 21 coherent signal bursts per second. Each burst consists of 64 pulses at a pulse repetition frequency of about 18 kHz. Using delay/Doppler processing (Raney, 1998), the echoes of each burst are separated along-track into 64 Doppler beams, illuminating narrow footprints of roughly 400 m along-track and 15 km across-track (half-power beam width). In the range direction, the measurement window spans about 240 m. As CryoSat-2 moves along its orbit, each ground location is observed by Doppler beams from successive bursts, typically yielding about 50 – 60 individual looks in SARIn mode. These are aligned and averaged to reduce noise ("multilooking"). The L1b product

https://doi.org/10.5194/egusphere-2026-5522
Preprint. Discussion started: 27 October 2026
© Author(s) 2026. CC BY 4.0 License.

provides about 20 multilooked "waveforms" per second, each containing the aggregated information for one ground location. The L1b data include power, coherence, and phase difference recordings in 1024 samples over the range window, potentially each bearing information about the surface at some location. Note that the data are oversampled by a factor of 2 and that neighboring samples are related to each other. If the recorded power is much larger than the noise, we attempt to recover the reflection's origin.

ESA also distributes processed elevations through CryoTEMPO-EOLIS (Gourmelen et al., 2018; Jakob and Gourmelen, 2023; CryoTEMPO-EOLIS, 2026). CryoSwath derives its elevations directly from the L1b waveforms.

2.2 Reference topography

We employ the digital elevation model (DEM) ArcticDEM 100 m mosaics at version 4.1 (Porter et al., 2023) to aid in locating the echo origins of CryoSat-2's signal. ArcticDEM is based on photogrammetry. We also use ArcticDEM to mitigate potential biases from changes in the data distribution by considering the differences between CryoSat-2-retrieved elevation estimates and ArcticDEM.

2.3 Glacier and drainage basin extents

We use the glacier basin extents given by the Randolph Glacier Inventory (RGI) version 7.0 (RGI 7.0 Consortium, 2023) to identify glacierized areas. Further, we use RGI data to summarize the presented data for first- and second-order regions as defined by the RGI. First-order regions, e.g., Alaska, can contain multiple second-order regions, e.g., North Alaska, Alaska Range, and more. We use the term region for first-order regions, while we refer to second-order regions as subregions. The studied regions are Alaska, Arctic Canada North and South, Greenland Periphery, Iceland, Svalbard and Jan Mayen, Scandinavia, and Russian Arctic. One exception, where we do not follow the RGI second-order convention, is the Greenland periphery. While in the RGI dataset, it constitutes a single subregion, we divide it into 5 subregions: North Greenland, West Greenland, Southwest Greenland, Southeast Greenland, and East Greenland. The lists of the RGI glacier and complex identifiers for each custom subregion are available (Sect. 7).

3 Algorithm

With the data described above, we are equipped to derive CryoSat-2 swath point surface elevation estimates and higher-order products, e.g., rasterized surface elevation change rates. We explain the algorithm in this section, starting from the input data, describing echo geolocation, resolving the phase ambiguity, rasterizing point elevation estimates, fitting a trend model, interpolating voids, and computing regional mass change time series. Echo geolocation and phase ambiguity resolution build on established swath processing methods (Gourmelen et al., 2018; Garcia-Mondéjar et al., 2019), with CryoSwath's modifications described below. The flowchart in Appendix Fig. A1 provides an overview of the workflow. Note that the most recent release of its Python implementation can be found on GitHub at `github.com/j-haacker/cryoswath`. CryoSwath can be installed

https://doi.org/10.5194/egusphere-2026-5522
Preprint. Discussion started: 27 October 2026
© Author(s) 2026. CC BY 4.0 License.

using the package managers pip or conda, or can be used inside a Docker container. The version used for the present data is 0.2.2.

3.1 Data selection

With the L1b data product, ESA provides indicators (flags) that help to recognize potentially bad data. We discard waveforms that are flagged with one or more of the "measurement confidence data" flags (`flag_mcd_20_ku`) stated in Table A1 (Scagliola and Geminale, 2020) to reduce the risk of polluting the dataset with erroneous measurements. While this is CryoSwath's default choice, it allows any user-defined selection. These are ESA's input flags; the coherence, power, and swath-start criteria below are CryoSwath's configurable filtering choices. To reduce computational costs, we exclude waveforms where the satellite's ground position is 30 km or further away from any glacier because the antenna gain is too small to receive any signal (< -40 dB, see Gray et al., 2013). Further, we ignore waveform samples for which the coherence is lower than 0.6. The coherence is close to 1, if a single, small area reflects much more of the signal than other sources. If, on the other hand, there are multiple areas reflecting similarly strong signals, the coherence is small with a minimum value of 0. Again, CryoSwath allows the user to choose the coherence threshold. CryoSwath further defaults to excluding samples before and just after the first peak of the coherence. The definition of the excluded part can be summarized as all samples before the coherence rises again after its first peak. This is an important step that separates the usable data from data that are especially prone to systematic errors (Haacker et al., 2023).

In the following, we express the range distance between waveform samples in meters because these distances also have physical meanings that relate to glacier surface properties, e.g., roughness. The distance between two adjacent waveform samples is 0.2342 m. The stated distances should be translated to waveform sample numbers by rounding down to the next lower integer. For example, if waveform sample number b is 5 m behind waveform sample number a in range direction, then $b = a + \mathrm{floor}(5/0.2342) = a + 21$.

CryoSwath uses a sophisticated algorithm that balances harvesting data and the risk of polluting the dataset by identifying the initial waveform part that is associated with returns from the POCA. Samples before that corresponding to the POCA should not be swath processed, since the POCA is the surface at the smallest range. Over oceans and flat parts of ice sheets, the location of the POCA-sample relative to the extent of the leading edge of the power waveform can be chosen such that the sample corresponds to an estimate of the elevation of the air-snow, -firn, -ice, or -water interface. Over mountain glaciers, this strategy is not easily applicable because the complex topography translates to a complex power waveform. Luckily, the coherence is a robust measure of the spatial scatterer density at the corresponding range that can be used alternatively. However, there are subtle differences in the interpretation: the first coherence peak, corresponding to the first large scatterer density, is not necessarily at the surface, but can be at a dense layer within the snowpack or firn (see section "scattering horizon" below). In the context of this layer, the first coherence peak marks the closest distance to the satellite and will here, in the context of swath processing, be treated like the conventional POCA. CryoSwath finds the first waveform sample that passes the coherence threshold (0.6 here). It identifies the POCA at the maximum coherence within 10 m (default value) after the first sample that exceeded the coherence threshold. After the POCA, the coherence first decreases before it starts to increase again (Gray et al.,

https://doi.org/10.5194/egusphere-2026-5522
Preprint. Discussion started: 27 October 2026
© Author(s) 2026. CC BY 4.0 License.

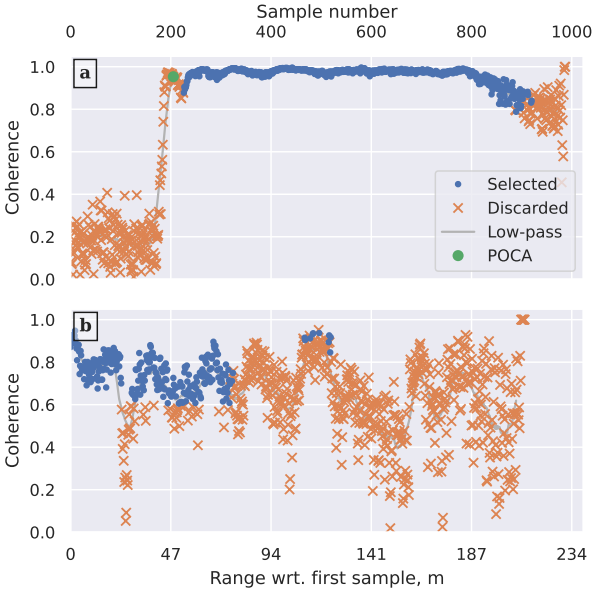

Figure 1. Exemplary coherence waveforms. The blue dots and the orange crosses show the coherence of each sample of the waveform. The blue-dot-samples will lead to point elevation estimates later, while the orange-cross samples will be discarded. The gray line shows the low-pass filtered coherence. The filled green circle indicates the coherence at the point of closest approach (POCA). Panel (a) shows an example of the regular case and panel (b) shows an example for a class of special cases where CryoSat-2 receives a signal starting from the first sample.

2013). The algorithm detects increases in the low-pass filtered coherence that exceed 0.001 per sample in the range between 5 and 55 m (default value) after the POCA sample. The detected sample is the first to be swath-processed, later referred to as "swath start". The mentioned waveform sections and samples are shown at hand of an example in Fig. 1a. Should no coherence increase be detected in the given range, the waveform is disregarded entirely.

If CryoSat-2 has misaligned the range window, it is possible that the window does not start before the first surfaces are illuminated. Such cases are recognized if the coherence threshold is exceeded in the first 10 m of the range window. Then, CryoSwath swath processes all samples, including those at the beginning of the waveform. An example of the case is shown in Fig. 1b.

Finally, we discard weak signals, i.e., waveform samples with a signal-to-noise ratio less than 10 (default value). The L1b product includes a noise power estimate for each waveform. However, the noise value is volatile and sometimes unrealistically high. In such cases, the signal-to-noise threshold can lead to disregarding waveform samples that do not appear to be noisy when inspected. By default, and as used for the present data, CryoSwath does not use the provided noise values but calculates the noise from the received signal power at the beginning of waveforms over the entire track. In detail, for each waveform, we calculate the average received power of the first 30 samples. We then calculate the minimum values for rolling windows of 100

https://doi.org/10.5194/egusphere-2026-5522
Preprint. Discussion started: 27 October 2026
© Author(s) 2026. CC BY 4.0 License.

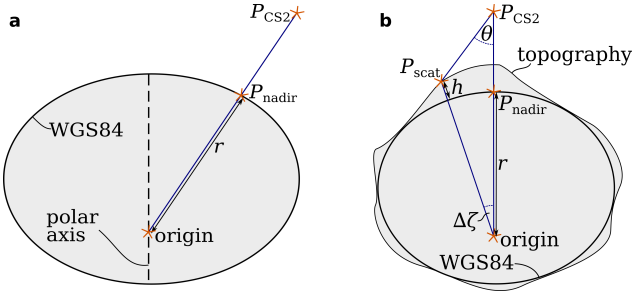

Figure 2. Two cross-sections, panel (a) along and panel (b) across CryoSat-2's track, that visualize P_{CS2}, P_{scat}, h, r, θ, and $\Delta\zeta$ that are used in the location of the echo origin. Additionally, the reference ellipsoid WGS84, the polar axis, nadir (on the reference ellipsoid), the origin of the reference frame, and the topography are indicated. Note that the measures are not to scale but are chosen such that meaningful distances are large enough to be recognized.

waveforms, corresponding to about 30 km along-track, in forward and backward directions. For each waveform, the larger of the two minimum values defines the noise power estimate.

3.2 Apparent echo origin location

Please refer to the sketch in Fig. 2 for visual guidance. Note that we can only retrieve the apparent, i.e., the calculated echo origin, which can differ from the actual one for a number of reasons (see Sect. 4). Further, note that the reference frame for the calculations is shifted such that its origin coincides with the intersection of the WGS84-normal at the satellite's coordinates and the polar axis. Vectors that describe points relative to the origin of this reference frame will be named $\boldsymbol{P}_{xxx}$, with xxx being some descriptive subscript.

We calculate the location of the echo origin from the position of the satellite $\boldsymbol{P}_{CS2}$, the satellite's travel direction α_{CS2}, the satellite-scatterer distance $\overline{P_{CS2}P_{scat}}$, and the nadir-scatterer angle θ, also known as angle of arrival. The satellite position $\boldsymbol{P}_{CS2}$ is given by the initial data as latitude ϕ, longitude λ, and height above the reference ellipsoid. CryoSat-2's travel direction α_{CS2} is estimated: we calculate the azimuths between all satellite positions of the current track extent; we then use a least-squares regression to fit a third-order polynomial to the azimuths; finally, we evaluate the polynomial at the location corresponding to the satellite's position. The satellite-scatterer distance $\overline{P_{CS2}P_{scat}}$ is calculated from the delay between transmitting and receiving the signal, the speed of light in vacuum, and the waveform sample number. We correct the distance $\overline{P_{CS2}P_{scat}}$ for the effects of the ionosphere, the dry and wet troposphere, and the pole, solid-earth, and load tides. Those corrections are provided with the L1b product. The angle θ is calculated from the roll angle χ, the distance between the two antenna centers b, the signal frequency f_{Ku}, and the phase difference $\Delta\beta$: $\theta = \arcsin\left(\frac{\Delta\beta \cdot c}{f_{Ku} \cdot 2\pi \cdot b}\right) - \chi$. The angle θ is on the order of 1 °.

The coordinate derivation is given in Appendix A1.

For the current dataset, actually, we low-pass filter the phase difference before calculating the echo origins as described above. We do so to mitigate the impact of noise on the later surface elevation aggregates of areas with low data density. The default used here is a Gaussian-weighted average over a rolling window of 21 samples with a standard deviation of 5 samples.

https://doi.org/10.5194/egusphere-2026-5522
Preprint. Discussion started: 27 October 2026
© Author(s) 2026. CC BY 4.0 License.

The chosen low-pass filter balances reducing fluctuations that increase when the received power decreases and maintaining a large number of independent elevation estimates by limiting the filter scope. We explored different filter settings, including no low-pass filtering, and found the results to be robust.

3.3 Phase ambiguity

We will use the phase difference recording to retrieve the echo location. Depending on the nadir-scatterer angle θ (Fig. 2), the echo travels different distances to each of the two antennas. This path length difference maps to a difference in the phase of the signal received at the antennas, measured by CryoSat-2's sensor. However, we cannot tell the absolute phase difference since it wraps at 2π. This introduces an ambiguity: the phase difference could be $n \cdot 2\pi$ "off", with $n \in \mathbb{Z}$. In consequence, there are a number of theoretically possible nadir-scatterer angles. To resolve this ambiguity, we compare the resulting possible scatterer locations to a DEM. We calculate possible locations for $n \in [-3..3]$ as described in Appendix A1 and deem the locations that are closer to the DEM more probable than those further away. In this section, we describe the implemented algorithm to choose n.

The algorithm is an extension of the work of Garcia-Mondéjar et al. (2019), previously published in Haacker et al. (2023). Basically, surfaces are assumed to be continuous and consecutive waveform samples are expected to differ only slightly in the phase difference. In practice, this assumption can be violated when the footprint simultaneously illuminates distinct surfaces (e.g. opposing valley slopes) and the dominant scattering contribution switches between them. The algorithm therefore splits the waveform where such switching is likely. This creates groups of samples, in which continuity is assumed. Two independent exceptions define where the waveform is split into groups. The first one typically occurs when two distinct surfaces separated by more than 5 km are illuminated together, and the second one on shorter distances.

The first exception is satisfied if (i) three or more consecutive samples either are excluded from swath processing because they do not meet the global coherence and power criteria, here 0.6 and ten times the noise power, respectively, or (ii) the sample's original phase difference, independent of the optional low-pass filtering (see above), deviates more than 0.1 rad from the smoothed reference. The power and phase difference thresholds prevent two types of signals from unintentionally connecting sample groups: signals that exceed the coherence threshold but are very weak, and signals that originate from a different location.

The second exception is satisfied if the smoothed reference changes faster than 0.1 rad between neighboring samples, or 0.16 rad from sample number i to $i+2$ (two times 80 $\%$ of 0.1 rad). CryoSwath allows modifying all thresholds, but any custom settings should be tested for the expected behavior because of their interdependency. Note that CryoSwath features diagnostic visualizations to inspect the waveforms, e.g., `cryoswath.test_plots.waveform.dem_transect()`.

The approach described above results in groups of waveform samples, resulting from cutting the waveform where the two mentioned exceptions occur. For each group and possible values for n, CryoSwath considers two measures: the median difference to the reference DEM, and the median absolute deviation (Höhle and Höhle, 2009) from the reference DEM. The first evaluates the difference from the expected surface elevation, and the second, whether the samples resemble the shape of the reference. Subsequently, n is chosen such that the sum of the squares of both is minimized. Therefore, those solutions that are

https://doi.org/10.5194/egusphere-2026-5522
Preprint. Discussion started: 27 October 2026
© Author(s) 2026. CC BY 4.0 License.

far from the reference, or those that disagree on the shape, are penalized. CryoSwath accepts custom functions for selecting the phase-wrap factor.

3.4 Rasterization of point data

After resolving the phase ambiguity, we arrive at point elevation estimates. This stage is often referred to as level 2 (L2) data. Each L1b waveform results in up to 1024 point elevation estimates; however, usually many (order 100) waveform samples are discarded by one of the filters described above (before swath start, low coherence, or low signal-to-noise ratio). Note that CryoSwath users can pass any variable from the L1b data to the L2 data. This can be used to inspect, e.g., the coherence or power that are used as quality indicators to filter the data (see above). In practice, the user would pass `retain_vars =["coherence_waveform_20_ku", "power_waveform_20_ku"]` to any function that returns L2 data, e.g., `cryoswath.l2.process_and_save()`.

For the remaining computation, we subtract the surface elevations of a reference DEM, here, ArcticDEM, from our derived point elevation estimates, resulting in the difference h_Δ. We consider these differences to mitigate a potential bias from an uneven distribution of data points over the surface. Absolute differences exceeding 150 m are discarded, i.e., all remaining satisfy $|h_\Delta| \leq 150\ \mathrm{m}$. Even when we do not explicitly say so, any reference to surface elevations refers to h_Δ.

We aggregate the L2 swath elevation data within 500 by 500 m grid cells and within a rolling three-month window, which we found to best balance resolution and uncertainty, resulting in level 3 (L3) data. First, we calculate the median of the elevation differences h_Δ. Further, to estimate the uncertainty of the median difference, we calculate the interquartile range of the differences and count the number of data points in each grid cell. While these are the default choices in CryoSwath, the spatial resolution, the temporal resolution, the aggregation period, the calculated statistics, and whether and which outliers should be excluded can be freely chosen by the user.

3.5 Computing elevation trends

For the rasterized elevation estimates, we derive the linear trend by least-squares fitting a model to the data. Note that we do not attempt to offer generic solutions for processing beyond L3 data. However, CryoSwath's modularity allows replacing or extending the implemented model. The model selected here contains, in addition to the trend parameter, a yearly and semi-yearly cycle. Its mathematical formulation follows in Eq. 1.

$$h_\Delta(t) = c + m \cdot t + A_{\text{full}} \cos(2\pi \cdot t - \phi_{\text{full}}) + A_{\text{semi}} \cos(4\pi \cdot t - \phi_{\text{semi}}) \tag{1}$$

In Eq. 1, the independent variable t is the time in years. Further, c denotes a constant offset, m is the surface elevation change trend, A_{full} and A_{semi} are the cycle amplitudes of the yearly and semi-yearly components, respectively, the indexed ϕ are the cycle phases with indices as before.

Grid cell time step aggregates that are based on less than 4 point elevation estimates or those, where the interquartile range is larger than 30 m, are excluded from further evaluation. We require that at least 5 of the 30 first and 5 of the 30 last time steps contain elevation estimates to exclude poorly sampled grid cells. We found the chosen values to form a consensus for all

https://doi.org/10.5194/egusphere-2026-5522
Preprint. Discussion started: 27 October 2026
© Author(s) 2026. CC BY 4.0 License.

studied regions, reducing the prevalence of poorly sampled time series while maintaining sufficient spatial coverage. Systematic optimization is not in the scope of the current study and would probably require an individual analysis of the regions. Those time steps for which the residual is larger than two standard deviations of the residuals of the grid cell in question are considered outliers and the model is fitted again, disregarding the outliers.

Subsequently, we exclude grid cells of which the trend parameter variance is larger than 2 $\mathrm{m}^2\ \mathrm{yr}^{-2}$ or either of the amplitude variances exceeds 100 m^2. The exclusion thresholds have been chosen empirically, striving to balance excluding seemingly implausible data while limiting false positives. This exclusion criterion, as well as the outlier-removal above, are not expected to bias trend estimates, but could, however, artificially lower the trend uncertainty estimate. Quantifying the choices' impacts is not in the scope of the current study. Note that it would require reference data in a variety of regions and during different seasons.

3.6 Void interpolation

There are voids in the spatial trend data and in the rasterized monthly elevation estimates. We fill voids for both kinds of data using almost the same method. We explain our approach below in detail, structured in processing "Steps". The data products include flags that indicate how each cell was filled, with directly observed data being indicated by a flag value of zero. The flag values mostly match the following Step numbers, however, with exceptions in Step 2 and 3. These output flags are distinct from ESA's input measurement-confidence flags used for data selection (Sect. 3.1).

Step 1: In a first step, for those grid cells where a model could be fitted (see previous section) all missing time step values in the monthly dataset are filled by evaluating the model. The uncertainty of the filled grid cells is estimated by two times the root-mean-square error of the fitted models. Concerned cells are flagged with the value one.

Step 2: Afterward, in both datasets, we attempt to mask areas that were ice-free most of the time. These areas would otherwise bias the later void-filling because they show no elevation change with a low uncertainty while not representing glacierized areas. The RGI glacier outlines contain ice-free areas because they represent the glaciers as they were around the year 2000, while the present dataset starts only in 2010. To determine which areas are mostly ice-free, we analyze average grid cell trends per elevation band for each basin. Elevation bands are chosen as required for the hypsometric interpolation in Step 3.2. In detail, they are chosen depending on the glacier's 10th to 90th percentile elevation span (10-90-span) according to the reference DEM. If the 10-90-span is less than 500 m, the bands are chosen such that they span one tenth of the 10-90-span. Else, the bands span 50 m. The lowest band is aligned with the lowest elevation of the glacier surface. For ice-free elevation bands, the average elevation trend is close to zero. If the lowest band is ice-free, the lowest glacierized band shows the largest absolute elevation trend. We search and find the maximum absolute average trend or elevation difference of the lowest five elevation bands for the trend dataset or the monthly dataset, respectively. The lowest band of which the absolute average trend or elevation difference is larger than half of the maximum is considered as the front of the glacier. Lower grid cells are excluded from further evaluation. The above assumes that the glacier either retreats or advances. If that is not the case, the average elevation trends of the five lowest bands are similar which leads to not excluding any data.

https://doi.org/10.5194/egusphere-2026-5522
Preprint. Discussion started: 27 October 2026
© Author(s) 2026. CC BY 4.0 License.

Step 3: The following Steps 3.1–3.5 are executed consecutively for individual basins (flag value two) and, then, for groups of basins (flag value 3) that are chosen along termination type, latitude, and longitude. More specifically, the termination types are read from RGI and are either "marine-terminating" or "unclassified". Further, the groups span about 1 ° latitude and 1 ° longitude divided by the cosine of latitude (to maintain the same scale across different latitudes). Repeating the Steps 3.1–3.5 for groups of basins is necessary if there are insufficient data for individual basins. In fact, there can be cases in which even for the basin groups the available elevation estimates are insufficient for a number of time steps or even for all. These cases are handled in Step 4, for the monthly dataset, and Step 5, for both datasets.

Step 3.1: We attempt to filter noise by comparing grid cells to their neighbors using the Z-score, i.e., a statistical measure of deviation. The Z-score is defined as the difference of a sample member to the sample mean, scaled by the sample standard deviation. We compare the Z-scores per grid cell of each dataset (trend data and monthly data) with the DEM-based elevation Z-scores. In detail, we calculate the Z-score in a 5 by 5 grid cell window, if this window contains 6 or more valid values. If the difference between the DEM Z-scores and each of the datasets is larger than two, we consider the grid cell in question a potential outlier and discard its value. By relating the dataset Z-score to the DEM Z-score, we dynamically adapt the noise threshold to the topographic complexity.

Step 3.2: We continue by aggregating data in preparation for applying the local mean hypsometric interpolation method (McNabb et al., 2019). The local mean hypsometric interpolation method fits a third-order polynomial to the average glacier elevation trends or differences of elevation bands and interpolates voids using the fitted model evaluated at the void's surface elevation. The surface elevations at the location of voids and of observations are read from a reference DEM. However, in many cases, the uncertainties of elevation trends or differences spread across more than one order of magnitude. We use a weighted average instead of the regular average, to mitigate the influence of values with a large uncertainty on the average. Here, the weights are the reciprocal trend-parameter variances from the fits described in Sect. 3.5 for the trend data, and the reciprocal interquartile range of point elevation estimates for the monthly data. Values that deviate more than two standard deviations from the weighted average are discarded as outliers. The effective number of observations that constitute the weighted average is defined by $\left(\sum_i w_i\right)^2 / \sum_i w_i^2$, with w_i denoting the weight of cell i. Thus, the effective number of observations is always lower than the actual number of observations, and it is largest for roughly equal weights. In the subsequent fit, we consider only those bands for which the effective number of observations is 6 or larger.

Step 3.3: For fitting the hypsometric model, we require weighted averages for at least five elevation bands. We use the ridge regression implementation of `scikit-learn` (Pedregosa et al., 2011; scikit-learn developers, 2026) with the singular value decomposition solver that allows weighting the observations, to fit the polynomial. Next to weighting the residuals which will be explained below, this approach is different from a regular least-squares regression because, in addition to the square-error, the sum of squared parameter values is minimized. A test using the regular least-squares method led to large values for the lowest and highest elevation bands for single basins, which seemed unrealistic because neighboring glaciers did not show similar behavior and no surge events, i.e., rapid acceleration of glacier flow speeds that can lead to fast changes of the surface elevation, were reported for the concerned glaciers. We choose the mentioned ridge regression to penalize models that deviate much from the equilibrium state, i.e., no elevation change across all bands. We weight residuals by the reciprocals of the

https://doi.org/10.5194/egusphere-2026-5522
Preprint. Discussion started: 27 October 2026
© Author(s) 2026. CC BY 4.0 License.

weighted variance for each elevation band divided by the effective number of observations. In case of the monthly data, we impose a threshold on the maximum absolute gradient of the third-order polynomial. This is necessary to avoid unrealistic polynomials in extreme cases, e.g., where a little weight is given to outer bands and a concentrated set of highly weighted bands forces large parameters for the second and third orders. We require the absolute gradient to remain lower than 10 m per 100 m of elevation. The hypsometric model is only fitted if there are data for 5 or more bands. If fewer or no data are available, we attempt to fill the concerned cells in the next larger scope.

Step 3.4: For elevations lower than the first elevation band for which we could derive a weighted average and for elevations higher than the highest valid band, we need to extrapolate the model. We extrapolate linearly, where the elevation lies no further outside the value-covered range than one third of this range, and where the linear extrapolation does not exceed the range of weighted averages including their uncertainty. Where one of the two conditions is violated, we extrapolate with the same value as the nearest valid band.

Step 3.5: Where the resulting hypsometric model with its linear or constant-value extrapolation differs from the earlier calculated 5 by 5 cell averages by more than two standard deviations, we fill voids with the local average. Otherwise, voids are filled by evaluating the hypsometric model. The uncertainty of the filled grid cells is estimated by two times the root-mean-square error of the fitted model.

Step 4: For the monthly dataset, we attempt to fill remaining voids temporally: Where the above method failed only for a subset of time steps, the successfully filled time steps are linearly interpolated to fill the missing time steps (flag value 4). We do not interpolate where the void periods are longer than one year.

Step 5: We proceed by applying Steps 3.1 to 3.5 to entire subregions for both datasets. The only difference is that elevation trends or differences that would be considered outliers following the above method, are not replaced but only excluded from the statistics. This acknowledges that cells of different basins may behave very differently depending on the basin's state, e.g., surging, recovering from a surge, or none of the previous two. The uncertainty of the filled grid cells is estimated by two times the root-mean-square error of the fitted models. Concerned cells are indicated by a flag value of five.

Step 6: If voids remain in the monthly dataset after the steps above, they are filled with the temporally closest value (flag value six). Then, we set the uncertainty to 74 m for the filled values. This seemingly specific number has no physical meaning but merely originates from converting a hypothetical interquartile range of 50 m—again without physical meaning but well higher than that of direct observations—to the equivalent standard deviation times two. Filling voids with the temporally closest value especially concerns June to October 2010 where CryoSat-2 was not yet fully operational and fewer tracks are available. The current Step 6 leaves no voids.

3.7 Elevation and mass change trends

We calculate regional and Arctic-wide time series by spatially averaging the monthly surface elevation estimates. First, we decimate the rolling-window time series by selecting every third month to remove elevation estimates that are directly related to others. Specifically, the selected months are November, February, May, and August. Next, we fit the model described in Eq. 1. In Fig. 3 (Sect. 5), we show the monthly data, the decimated data, the data with the seasonal signal removed, and

https://doi.org/10.5194/egusphere-2026-5522
Preprint. Discussion started: 27 October 2026
© Author(s) 2026. CC BY 4.0 License.

the fitted trend for the Arctic-wide glacier surface elevation change. We test the significance of the trend using a Student's t-test. For our 2010–2024 time series of 58 3-monthly intervals, the 52 degrees of freedom remain, accounting for 6 fitted parameters. For 52 degrees of freedom, the t-test rejects the null hypothesis of no significant trend for t values exceeding ± 2.006 at $\alpha = 0.05$ (two-sided). We convert the elevation changes to mass changes assuming the average density of glacier volume changes $\rho = 850 \pm 60\ \mathrm{kg\ m^{-3}}$ (Huss, 2013).

4 Errors and uncertainties

4.1 Location errors

Errors in the location of echo origins are the dominant source of uncertainty for CryoSat-2 swath elevation estimates. Here, we briefly discuss three contributors: (a) n was chosen incorrectly in the phase unwrapping, (b) phase difference uncertainty, and (c) range-ambiguity (superposition) errors.

(a) Wrong phase-wrap factors affect very few data points because it requires better agreement with the reference DEM at one of the ambiguous locations. If there were multiple surfaces at similar ranges in the footprint, the signal coherence is low (except one of the surfaces reflects the signal substantially better) and the concerned waveform samples are discarded by the coherence filter. Groups are even less likely to be affected because the majority of group members would need to fit the ambiguous location better, implying the ambiguous location not only accidentally fits with regard to the average elevation, but also fits with regard to the topography.

(b) Noise in the phase difference results in a location error in the across-track direction, typically between 50 and 150 m before low-pass filtering. These numbers are based on an analysis of samples with coherence larger than 0.95 to exclude type-(c) errors (see below), and low power where the noise is largest. Errors from noise become small when multiple points are averaged (Johnson and Dudgeon, 1993, Ch. 1).

(c) Range-ambiguity errors result from multiple coherently interfering echoes, a common case close to summits or in valleys (Haacker et al., 2023). Affected waveform samples have a reduced coherence, such that the largest errors are discarded by the filter. However, the errors are still in the order of 10 m, systematic, and affect consecutive waveform samples similarly. Haacker et al. (2023) concluded that this error can be reduced by averaging all available data from 89 days and that comparing data separated by one or multiple years reduces the error. In the current work, we aggregate elevation estimates in 3-month rolling windows, matching the 89 days approximately. We do not restrict ourselves to only comparing yearly elevation estimates because the overall uncertainty for the aggregated regions are sufficiently small. Restricting the data to yearly differences would come at the cost of losing insights into seasonal variations.

Commonly, location errors show as elevation errors in the data. This is important to be aware of when interpreting this data product. However, the imposed coherence threshold and the consecutively applied maximum elevation difference filter mitigate the impact of the errors on the data product.

https://doi.org/10.5194/egusphere-2026-5522
Preprint. Discussion started: 27 October 2026
© Author(s) 2026. CC BY 4.0 License.

4.2 Scattering horizon

The transmitted Ku-band radar signal is reflected by matter depending on its electromagnetic properties. Water, as well as firn, ice, and snow (to some extent) reflect Ku-band radar. In general, two phenomena that play a role in reflecting the radar signal are distinguished, namely, surface scattering and volume scattering. "Surface scattering" describes the scattering at the surface due to the abrupt change in the refractive index at the air-ice/snow interface. The part of the radar wave that penetrates the surface is subject to "volume scattering", i.e., it is scattered within the firn/snow volume by, e.g., internal layers, grain-size contrasts, or ice lenses. Dry snow reflects little of the Ku-band radar signal and, usually, can be thought of as being transparent, while layers of wet and dense snow are not penetrated if they are thick enough.

With CryoSat-2, we can only observe the average echo for each waveform sample. This results in a scattering horizon that, usually, is between the snow-air interface and the glacial ice (Gray et al., 2019). The variable scattering horizon introduces a temporally correlated bias that can also be spatially correlated and elevation dependent. While often regarded as a source of uncertainty when considering elevation changes, it was hypothesized to provide novel insights: e.g., Morris et al. (2020, 2022) suggests the scattering horizon change could be used to estimate the winter snow cover thickness.

In summary, the observed surface elevation does not represent the snow-air interface and the signal's penetration depth depends on the climatic history. Thus, measurements of the same season are most comparable because the mass above the scattering horizon is least different. Similar to acknowledging the systematic location errors, type-(c), users should be especially cautious when interpreting absolute elevation estimates, or relative differences on time scales shorter than one year.

4.3 Elevation uncertainty

The complex relation between point elevation estimates and the rasterized monthly elevation estimates does not permit using standard procedures to derive the uncertainties. The major obstacle is the multimodal distribution of elevation estimates within grid cells. We estimate the uncertainty from the data spread given by the interquartile range scaled to the equivalent of two standard deviations. The range-ambiguity errors are already included, if points of multiple tracks are aggregated, as with the 3-monthly aggregation period of the current study.

When grid cells are spatially averaged, we consider a spatial correlation distance of 2 km (Jakob and Gourmelen, 2023) for observed grid cells to compute the uncertainty u_{obs}. Specifically, we sum the grid cell elevation uncertainties $u_{i,j}$ of 2 by 2 km patches arithmetically, then compute the root sum of squares across all patches, and divide through the number of observed grid cells N (Eq. 2).

$$u_{\mathrm{obs}} = \frac{1}{N}\sqrt{\sum_{\mathrm{patches}}\left(\sum_{i=1}^{4}\sum_{j=1}^{4} u_{i,j}\right)^2} \tag{2}$$

Errors in interpolated grid cells are correlated and biased with regard to observed grid cells. We estimate bias and correlation based on ArcticDEM strips. For each first-order region, we sample 10 randomly chosen points and, again randomly, select 10

https://doi.org/10.5194/egusphere-2026-5522
Preprint. Discussion started: 27 October 2026
© Author(s) 2026. CC BY 4.0 License.

ArcticDEM strips covering the sample point at different epochs, giving 100 strips in total, except for Alaska and Scandinavia where only about 90 strips were available for each region. We filter potentially compromised strip data excluding data where the provided data quality flag is not zero. Further, we downsample the 2 m resolution strip data using a two-step approach. Before storing the data, we average to 32 m, which greatly reduces storage requirements. Then, we average to our 500 m grid spacing. In this reference data, we observed large differences to the companion ArcticDEM mosaic product. We exclude these features by filtering the strip data based on rolling 5 by 5 cell patches. We exclude patches where either one value is more than 150 m different from the mosaic or where the minimum and maximum difference from the mosaic are further apart than 150 m. For each ArcticDEM strip we compare the strip elevations with the CryoSat-2-based elevation product at the time step closest to the strip acquisition date. The CryoSat-2 product contains both directly observed elevations and elevations that were filled using one of the interpolation methods. For every strip we therefore compute the mean elevation difference between the CryoSat-2 product and the ArcticDEM strip separately for (i) grid cells based on direct CryoSat-2 observations and (ii) grid cells whose values were obtained using each interpolation method. This yields one bias estimate per strip for the observed data ($b_{\text{ref}|0}$) and for each interpolation method ($b_{\text{ref}|1..6}$). The differences $b_{0|1..6} = b_{\text{ref}|1..6} - b_{\text{ref}|0}$ then estimate the bias of each interpolation method relative to the observed data. Aggregated by region, these differences are shown in the appendix Fig. A2. However, regional differences are small, and we do not treat regions differently going forward. We derive the uncertainties of interpolated data relative to observed data from the interquartile range scaled to the equivalent of two standard deviations $2\sigma_{0|1..6}$. Further, we calculate their correlations $R_{i,j}$ across all strips. The uncertainty of spatially aggregated elevation estimates $u_{\text{sp.agg.}}$ is then given by Eq. 3, where u_{obs} is based on point-measurement interquartile ranges scaled to two standard deviations (see above), A_i is the area that was interpolated with method i, and A is the total aggregated area.

$$u_{\text{sp.agg.}} = \frac{1}{A}\sqrt{\left(u_{\text{obs}}A_{\text{obs}}\right)^2 + \sum_{i=1}^{6}\sum_{j=1}^{6}\left(R_{i,j}\cdot 2\sigma_{0|i}A_i \cdot 2\sigma_{0|j}A_j\right)} \tag{3}$$

Further, the errors are temporally correlated, which we consider in the uncertainties of inter-year mass change estimates below. For each of the sampled points, for each strip pair combination, we compute the correlation of the bias, i.e., the differences of the current product to the strips. The median correlation of biases across all pairs separated by one year is $R_{1\text{yr}} = 0.70$ (see appendix Fig. A3). The uncertainty $u_{t0,t1}$ of mass change estimates between year $t0$ and $t1$ is then given by Eq. 4.

$$u_{t0,t1} = \sqrt{u_{t0}^2 + u_{t1}^2 - 2R_{1\text{yr}}u_{t0}u_{t1}} \tag{4}$$

4.4 Uncertainty from glacier outlines

The glacier outlines from the RGI target the glaciers' extents at the year 2000 but can be a few years earlier or later (RGI 7.0 Consortium, 2023, standard deviation between 2 and 3 years). However, our observational period covers 2010 until 2024. We implemented an approach to detect glacier-free area where there are no seasonal elevation changes at the glacier front (Sect. 3.6, Step 2). We treat the area identified as ice-free because of glacier retreat as fully uncertain.

https://doi.org/10.5194/egusphere-2026-5522
Preprint. Discussion started: 27 October 2026
© Author(s) 2026. CC BY 4.0 License.

Moreover, four subregions were omitted completely due to insufficient data coverage. These are North Alaska, Alaska Peninsula (Aleutians), Labrador, and Jan Mayen, accounting for 0.4, 2.2, 0.05, and 0.3 % of their parent regions, respectively. For results for RGI first-order regions, we extrapolate the specific mass balance of the observed area to these subregions that are entirely missing from our trend product, using their glacier area from the RGI. We assume this extrapolation to be fully uncertain, i.e., the contribution from the extrapolated area is allowed to range from zero to twice the extrapolated value.

We combine omitted subregions and retreat-related ice-free areas in a single catch-all area uncertainty term, u_{A1}, because both contribute to the area mismatch between our trend product and the RGI. Specifically, u_{A1} is defined as the area difference between the glacier area covered by our trend product and the glacier area according to the RGI (Table A2). When subregions are aggregated, we assume these errors are fully correlated and sum them arithmetically. Expressed relative to the glacierized area of each RGI first-order region, u_{A1} ranges between 0.2 % for Arctic Canada South and 5.0 % for Svalbard and Jan Mayen.

Additionally, the outlines of glaciers from the RGI are inherently imperfect. For the outdated RGI version 3.2, the estimated uncertainties of the glacierized areas in regions of the Arctic except Scandinavia range from 2.5 % for Iceland to 4.6 % for Greenland Periphery (Pfeffer et al., 2014, updated for RGI v7.0 outlines). Scandinavia's glacier areas are uncertain to 9.2 %. In absence of a systematic uncertainty evaluation of the glacier areas in the current RGI version 7.0, we use the older uncertainty estimation, specifically, the area-dependent Eq. 5 with (individual) glacier area s_i and parameters $k = 3$, $e_1 = 0.039$, and $p = 0.70$ (Pfeffer et al., 2014, Eq. 1). This uncertainty estimate is assumed to be regionally (RGI first-order regions) correlated (Pfeffer et al., 2014), and is summed arithmetically resulting in u_{A2} with i in $1, .., N$ for N glaciers in the concerned region (Eq. 6, Table A2). The total area uncertainty u_A is calculated in Eq. 7.

$$e(s_i) = k e_1 s_i^p := 3 \cdot 0.039 \cdot s_i^{0.70} \tag{5}$$

$$u_{A2}(s_1, .., s_N) = \sum_i e(s_i) \tag{6}$$

$$u_A = \sqrt{u_{A1}^2 + u_{A2}^2} \tag{7}$$

4.5 Uncertainty propagation to higher-level results

We estimate the uncertainties of multi-year average surface elevation trends $u_{\dot{h}}$ by two standard deviations of the fitted model parameter (Sect. 3.7). Assuming a density uncertainty of glacial ice volume changes for long time scales $u_{\rho,\text{long}} = 60$ kg m^{-3} (Huss, 2013), the mass balance ($\dot{M}$) uncertainty $u_{\dot{M}}$ follows in Eq. 8 from uncertainty propagation, with the surface elevation trend $\dot{h}$ and other symbols like above.

$$u_{\dot{M}} = \sqrt{(A\rho \cdot u_{\dot{h}})^2 + (A\dot{h} \cdot u_{\rho,\text{long}})^2 + (\rho\dot{h} \cdot u_A)^2} \tag{8}$$

Further, we compute mass changes in single hydrological years which we define to start in September. For single years, we assume a larger density uncertainty of $u_{\rho,\text{short}} = 150$ kg m^{-3} (Huss, 2013). For the mass change from year $t0$ to year $t1$ with elevation change $\Delta h_{t0,t1}$, Equation 9 follows from propagating the uncertainties.

$$u_{\Delta M} = \sqrt{(A\rho \cdot u_{t0,t1})^2 + (A\,\Delta h_{t0,t1} \cdot u_{\rho,\text{short}})^2 + (\rho\,\Delta h_{t0,t1} \cdot u_A)^2} \tag{9}$$

https://doi.org/10.5194/egusphere-2026-5522
Preprint. Discussion started: 27 October 2026
© Author(s) 2026. CC BY 4.0 License.

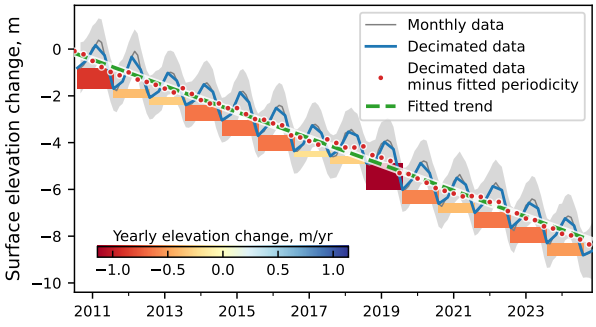

Figure 3. Arctic-wide average surface elevation change relative to August 2010 (seasonal signal removed) of the shown fitted model. The patches below the lines indicate the surface elevation change between two consecutive hydrological years.

For single-year mass changes, the elevation change uncertainty is about 20 to 100 times larger than the other contributions.

5 Results

The trend and monthly data products are published in georeferenced TIFF and netCDF formats, respectively, with each subregion in a separate file. The data are projected onto coordinate systems listed in Table A2 at a spatial resolution of 500 by 500 m. The trend product contains the trend data according to Sect. 3.5 and its standard deviation. The monthly product's main variable is the surface elevation difference from ArcticDEM. Additionally, we provide the standard deviation and the number of point elevation estimates that the aggregates are based on. Note that, while we consistently use 2σ-uncertainties in the current manuscript, the dataset follows NetCDF Climate and Forecast (CF) Metadata Conventions version 1.12 (Eaton et al., 2024) and includes a single standard deviation, as also specified in the metadata. Further, the dataset includes the reference elevation that the elevation differences refer to, the number of aggregated point measurements, and a flag that indicates the applied interpolation strategy. See the data availability section and the corresponding data description at the repository for the metadata in full detail.

For comparison, the EOLIS monthly gridded product described for Baseline 3 uses a 2 km grid and a three-month rolling window, and includes elevation uncertainty. Its point product combines swath and POCA observations, identified by an `is_swath` variable (CryoTEMPO-EOLIS, 2026), whereas our dataset is swath-only. Finer grid spacing does not by itself establish greater observational accuracy.

5.1 Arctic-wide results

Arctic-wide, we find an average glacier surface elevation trend of -0.56 ± 0.01 m yr^{-1} ($p \ll 10^{-3}$), corresponding to a glacier mass trend -197 ± 10 Gt yr^{-1}. Figure 3 shows the Arctic-wide trend and all components used to derive it (see Sect. 3.7) separately for clarity. Moreover, Fig. 3 highlights the yearly elevation changes. The melt season of the hydrological year

https://doi.org/10.5194/egusphere-2026-5522
Preprint. Discussion started: 27 October 2026
© Author(s) 2026. CC BY 4.0 License.

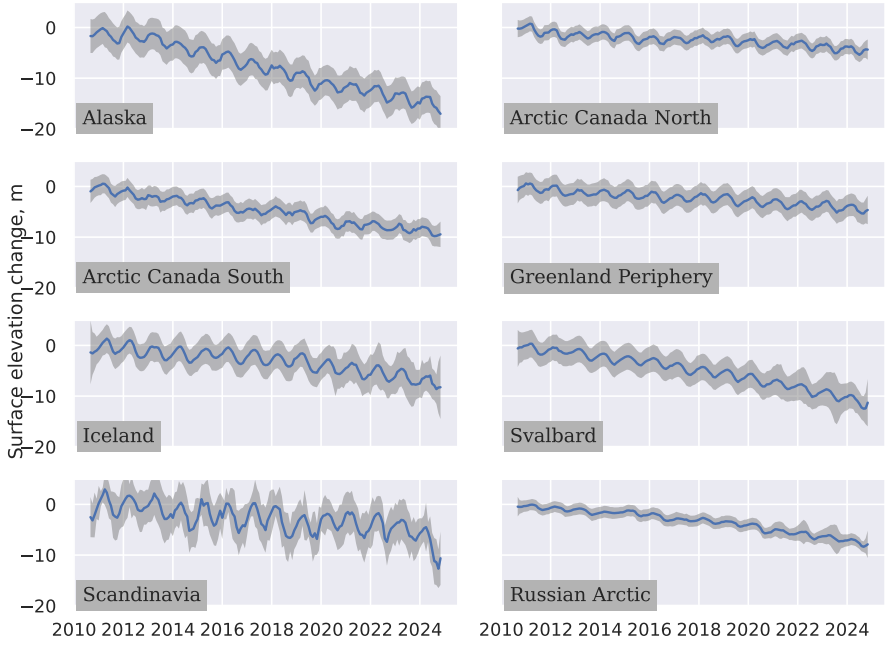

Figure 4. Average glacier surface elevation changes of each region. The change values refer to the August-2010-value of the model described in Eq. 1 (trend plus yearly and semi-yearly cycles), fitted to elevation estimates of the current region. The gray bands around each time series indicate 2σ-uncertainty intervals.

2018/19 stands out with a mass loss of 400 ± 260 Gt. This record mass loss has been attributed to anomalously warm air temperatures, transported from lower latitudes through persistent pressure systems in the Arctic (Wolken et al., 2020). However, the uncertainty of the single year mass balance is comparable to the value, or even larger in the case of individual regions. In absolute terms, with 159 ± 185 Gt Alaska contributed most to the overall ice loss in 2018/19. Collectively, Arctic Canada North (74 ± 99 Gt), Arctic Canada South (55 ± 53 Gt), and Greenland Periphery (56 ± 127 Gt) lost 186 ± 170 Gt in 2018/19. Figure 4 shows the time series of average surface elevation changes for each region.

The trends for each first-order RGI region are summarized in Table 1. The table includes a comparison of the periods August 2010 until August 2014 and August 2020 until August 2024. Statistically significant changes were found for Arctic Canada South, Iceland, Svalbard, Scandinavia, and Russian Arctic ($p < 0.05$). The periods were chosen to start in August for consistency with the chosen time steps (Sect. 3.7) and good alignment with the hydrological years (September to August).

5.2 Scandinavia

Scandinavia's glaciers thin at 0.48 ± 0.07 m yr^{-1} (Fig. 5, Table 1). We report the thinning rates of the seven largest ice caps separately in Table 2. Compared to other regions, the surface elevation shows a larger yearly cycle. The sensor provides sufficient data to estimate elevation trends directly, without interpolation, for nearly half of the glacierized area (46 % Southeast,

https://doi.org/10.5194/egusphere-2026-5522
Preprint. Discussion started: 27 October 2026
© Author(s) 2026. CC BY 4.0 License.

Table 1. Average mass-balance rates and surface elevation trends per RGI o1 region. The two columns titled "Period comparison" show values for the first and last four hydrological-year (September to August) periods. The penultimate column shows the average mass-balance rate from August 2010 until December 2019 for comparison with the reference in the last column. The final, separated column shows reference mass balances from January 2010 until December 2019 (Hugonnet et al., 2021). The value precision is given depending on the uncertainties order of magnitude ($\log_{10}$).

	Mass balance	Surface trend	Period comparison		Reference comparison	
	Aug 2010 – Nov 2024		2010 – 2014	2020 – 2024	2010 – 2019	
Region	$\mathrm{Gt\ yr^{-1}}$	$\mathrm{m\ yr^{-1}}$	$\mathrm{Gt\ yr^{-1}}$	$\mathrm{Gt\ yr^{-1}}$	$\mathrm{Gt\ yr^{-1}}$	$\mathrm{Gt\ yr^{-1}}$
Alaska	-80 ± 8	-1.103 ± 0.030	-54 ± 15	-66 ± 10	-82 ± 9	-79 ± 6
Arctic Canada North	-22.9 ± 2.8	-0.267 ± 0.022	-38 ± 16	-29 ± 8	-22 ± 5	-32.0 ± 2.7
Arctic Canada South	-22.0 ± 2.0	-0.640 ± 0.022	-26 ± 5	-15 ± 4	-21.9 ± 2.2	-29.4 ± 2.4
Greenland Periphery	-22.5 ± 2.2	-0.298 ± 0.015	-30 ± 8	-25 ± 4	-20.4 ± 2.9	-35 ± 4
North Greenland	-10.1 ± 1.0	-0.346 ± 0.014	-11 ± 3	-10.9 ± 1.8	-8.9 ± 1.1	
West Greenland	-4.1 ± 0.5	-0.48 ± 0.04	-6.4 ± 1.7	-1.7 ± 1.6	-4.8 ± 0.7	
Southwest Greenland	-3.5 ± 0.4	-0.61 ± 0.04	-5.4 ± 1.1	-1.4 ± 0.7	-4.0 ± 0.5	
Southeast Greenland	-1.3 ± 0.3	-0.24 ± 0.05	-2.4 ± 1.7	-6.1 ± 1.1	-1.1 ± 0.4	
East Greenland	-3.4 ± 0.8	-0.130 ± 0.027	-5 ± 5	-5 ± 4	-1.6 ± 1.4	
Iceland	-4.5 ± 0.5	-0.49 ± 0.03	-4.2 ± 1.2	-6.5 ± 1.3	-3.2 ± 0.5	-7.7 ± 0.6
Svalbard and Jan Mayen	-21.4 ± 2.1	-0.774 ± 0.027	-19 ± 3	-28 ± 3	-18.3 ± 1.9	-13.3 ± 1.1
Scandinavia	-1.20 ± 0.22	-0.48 ± 0.07	-0.7 ± 0.8	-2.9 ± 1.1	-1.24 ± 0.28	-1.50 ± 0.20
Russian Arctic	-22.0 ± 2.2	-0.523 ± 0.026	-17.1 ± 3.0	-28 ± 4	-16.9 ± 1.9	-11.8 ± 1.1
Arctic-wide	-197 ± 10	-0.563 ± 0.010	-188 ± 24	-200 ± 15	-185 ± 11	-210 ± 9

Table 2. Thinning rates of Scandinavia's largest glaciers from August 2010 to November 2024 in $\mathrm{m\ yr^{-1}}$.

Glacier	Thinning rate
Hardangerjoekulen	0.42 ± 0.10
Jostedalsbreen	0.39 ± 0.14
Soendre Folgefonna	0.57 ± 0.11
Nordre Folgefonna	0.52 ± 0.24
Svartisen-Vestisen	0.37 ± 0.10
Svartisen-Oestisen	0.35 ± 0.10
Blaemanissen	0.53 ± 0.11

515 49 % Southwest, 47 % North Scandinavia). The agreement with Hugonnet et al. (2021) (Table 1), also spatially (not shown), lends further credibility.

EOLIS includes Scandinavian point elevations, but Scandinavia is absent from the monthly gridded-product list in handbook Issue 4.1 (CryoTEMPO-EOLIS, 2026). Our dataset provides monthly sampled elevations on a 500 m grid.

https://doi.org/10.5194/egusphere-2026-5522
Preprint. Discussion started: 27 October 2026
© Author(s) 2026. CC BY 4.0 License.

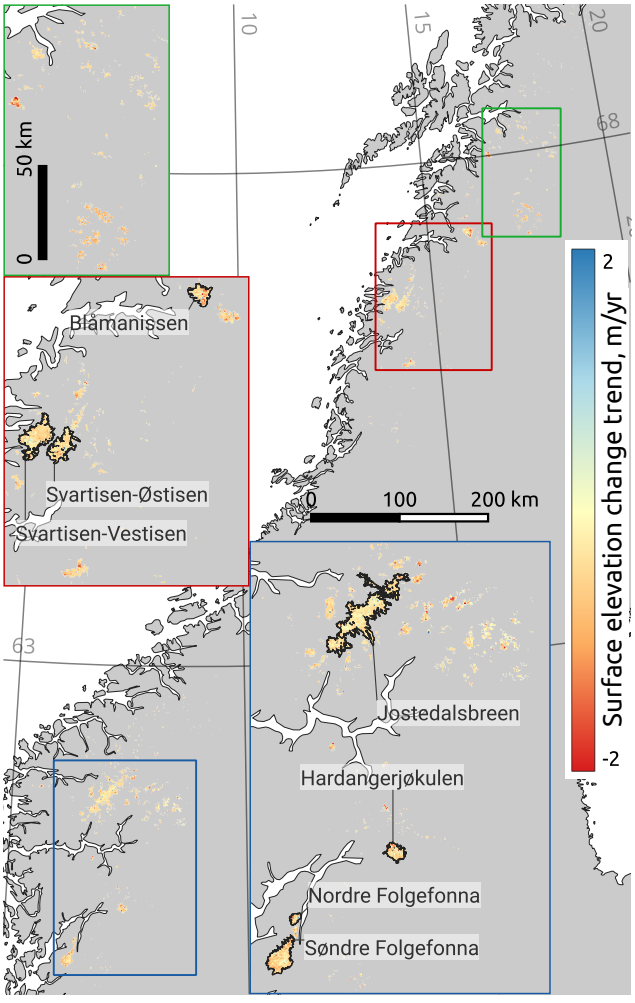

Figure 5. Scandinavian glaciers' thinning rate during 2010 – 2024. The three insets share the scale shown in the green inset.

6 Discussion

Global glacier elevation and mass changes were derived earlier using CryoSat-2 swath data from August 2010 to August 2020 (Jakob and Gourmelen, 2023). In all regions, our results for the period from August 2010 until August 2020 agree well with the earlier results (Table 3). By contrast, the results of a dataset from photogrammetry at 100 m resolution (Hugonnet et al., 2021) differ from the current study for a number of regions (Table 1). The relative difference is largest for Iceland where they find a -7.7 ± 0.6 $\mathrm{Gt\ y^{-1}}$ mass-balance rate from January 2010 until December 2019, while we only find -3.2 ± 0.5 $\mathrm{Gt\ yr^{-1}}$ for a similar period from August 2010 until December 2019. The good agreement with the earlier CryoSat-2-based study of Jakob and Gourmelen (2023) hints at sensor differences as the central cause for the discrepancy with the photogrammetry dataset of Hugonnet et al. (2021). We will, however, take a closer look because a constant bias between the compared methods could not

https://doi.org/10.5194/egusphere-2026-5522
Preprint. Discussion started: 27 October 2026
© Author(s) 2026. CC BY 4.0 License.

Table 3. Comparison of regional long-term mass-balance rates from the current study with an earlier study that also used swath-processed CryoSat-2 data (Jakob and Gourmelen, 2023, abbreviated as JG23 below). The observational period was August 2010 until August 2020. The values are given in gigatonnes per year. Scandinavia is not included in JG23 and cannot be compared. The uncertainties reported for JG23 use one standard error of fitted elevation trends, whereas CryoSwath values use two. The volume to mass conversion uncertainty estimate is the same for both studies, and the area uncertainty only differs slightly.

Region	CryoSwath	JG23
Alaska	-83.0 ± 9.0	-83.1 ± 7.6
Arctic Canada North	-22.0 ± 4.0	-23.2 ± 1.9
Arctic Canada South	-22.6 ± 2.2	-23.4 ± 2.0
Greenland Periphery	-21.1 ± 2.8	-23.8 ± 2.0
Iceland	-3.5 ± 0.5	-3.5 ± 0.3
Svalbard and Jan Mayen	-18.7 ± 1.9	-18.4 ± 1.6
Russian Arctic	-17.6 ± 1.9	-18.4 ± 1.0

explain the different change rates. Both datasets, the CryoSat-2- and the photogrammetry-based, use the same volume change density assumption; hence, we can rule this out as a cause for the observed difference. We continue by comparing the two datasets spatially for the ice cap Vatnajökull, Iceland, in the period 2010 until 2019 (Fig. 6). This ice cap accounts for about 70 % of the glacierized area in Iceland. We find a considerable difference in the overall mass-balance rate of $3.5\ \mathrm{Gt\ yr^{-1}}$ ($-1.9\ \mathrm{Gt\ yr^{-1}}$ CryoSat-2 vs $-5.3\ \mathrm{Gt\ yr^{-1}}$ photogrammetry). The majority of the large, positive deviations occur where the CryoSat-2 data were interpolated (Fig. 6). Especially a large fraction of grid cells at glacier fronts that mostly show a strong positive bias, were interpolated. Averaged over interpolated grid cells, the difference in mass-balance rates is $0.8\ \mathrm{Gt\ yr^{-1}}$, constituting 22 % of the overall difference that could be due to a biased interpolation that we will continue to discuss below. Another 18 % of the difference can be attributed to areas outside the coverage of the CryoSwath data. Of this 18 %, 2 % are from areas outside of the RGI ice cap outlines and 16 % are from areas that we excluded because they were flagged as not continuously glacierized. Further, 7 % are due to the 5 % most negative and 5 % most positive differences. Figure 7 visualizes the comparison of the trends in a two-dimensional histogram. A hypothetical upward shift of the scattering horizon could partly explain the remaining bias of $0.39\ \mathrm{m\ yr^{-1}}$ across the directly observed grid cells excluding the 5 %-tails. The difference patterns in Fig. 6 could potentially be exploited to gain insights into changes of the structure of upper snow/firn layer. However, the required research lies outside the current scope.

The coverage, which we define as the proportion of observed trends (as opposed to interpolated trends) to the total number of glacierized grid cells, varies much between regions. The coverage of Alaska Range (Wrangell/Kilbuck) is the lowest with 14.1 %; the coverage of Melville Island, Arctic Canada North, is the highest with 95.5 %. Next to the operational mode (SARIn or other) and the meridional track convergence, the fraction of the glacier surface inside the considered footprint that is illuminated by CryoSat-2's signal determines the coverage. Simplifying, if the range of elevations within the footprint

https://doi.org/10.5194/egusphere-2026-5522
Preprint. Discussion started: 27 October 2026
© Author(s) 2026. CC BY 4.0 License.

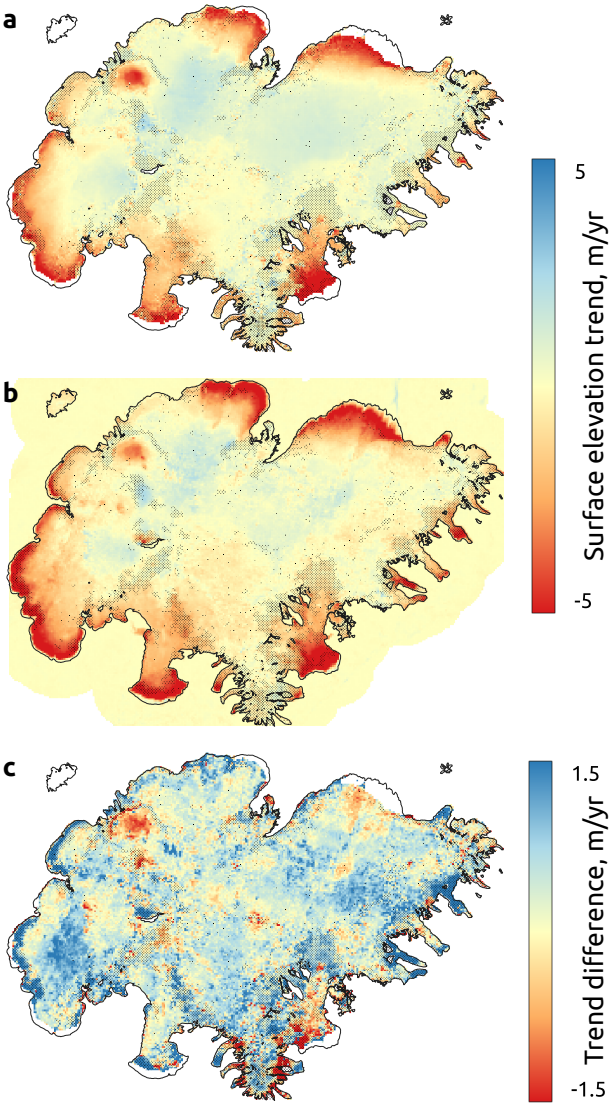

Figure 6. Surface elevation change trend of the CryoSat-2-based dataset (Panel a), of the photogrammetry dataset (Panel b, Hugonnet et al., 2021), and the difference between the two (Panel c) for the ice cap Vatnajökull in Iceland. Where the CryoSat-2 trends were not observed but interpolated, all three panels show a dotted hatching. Notably, positive differences prevail (Panel c, bluish colors). While the strongest differences occur where trends were interpolated, these explain only 22 % of the overall difference (see main text).

is less than 240 m, in an ideal case, CryoSat-2 could sample the entire surface. However, if the elevation range is larger, this is no longer possible. To visualize the actual relation between coverage and the elevation range in Fig. 8, we define a terrain complexity index that we refer to as footprint topography 10-90-span. This is the elevation difference between the tenth percentile and the 90th percentile of the surface hypsometry within each 15 by 15 km square that includes glaciers. Least-

https://doi.org/10.5194/egusphere-2026-5522
Preprint. Discussion started: 27 October 2026
© Author(s) 2026. CC BY 4.0 License.

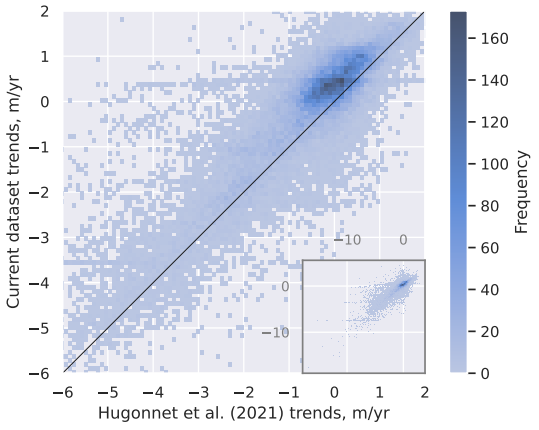

Figure 7. Two-dimensional histogram of the surface elevation change trends of the current CryoSat-2-based dataset and the earlier photogrammetry dataset (Hugonnet et al., 2021) per-cell for the ice cap Vatnajökull in Iceland. The black diagonal indicates the line of equality. The inset shows a larger extent that includes all data (2.7 % lie outside the main panel).

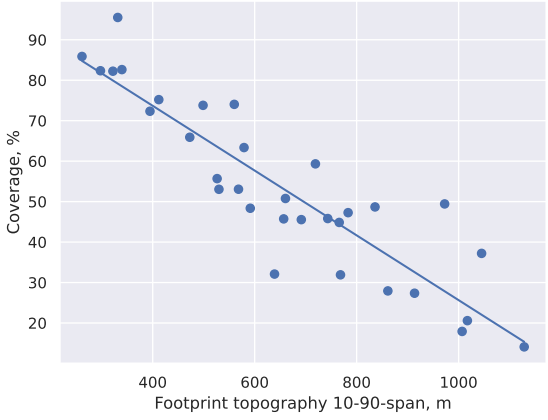

Figure 8. Percentage of directly observed grid cells with regard to a terrain complexity index, the footprint topography 10-90-span (see main text). Each point shows the aggregates for one subregion and the line shows a linear model fit. The coverage decays with increasing 10-90-span.

squares fitting a linear model to the data results in -8.0 ± 1.4 % coverage per 100 m of 10-90-span ($p \ll 0.05$). The lack of coverage is, at least roughly, proportional to the terrain complexity index. Together with the offset of 106 ± 10 % coverage for a hypothetical zero inter-quantile range (10-90-span), this insight could be used to estimate the expected CryoSat-2 SARIn coverage for other regions. However, extrapolating this estimate to other regions should be limited to comparable latitudes, i.e., poleward of about $\pm 60°$, and the here covered terrain complexities.

https://doi.org/10.5194/egusphere-2026-5522
Preprint. Discussion started: 27 October 2026
© Author(s) 2026. CC BY 4.0 License.

Earlier, we concluded that a part of the disagreement with reference data (22 % in the case of Vatnajökull) can be attributed to a biased interpolation. We interpolate voids using the state-of-the-art local mean hypsometric interpolation that has been found to perform best by McNabb et al. (2019). Our implementation adds weighting and ridge regularization (Sect. 3.6) to this approach. The underlying method bins elevation change data corresponding to bands of elevation in which the changes occur, fits a third-order polynomial to the changes, and integrates the fitted model folded with the hypsometry. Despite being the best established method, it has not been evaluated specifically for radar altimetry data. We find that no data being available for the highest or lowest elevation bands complicates this method because the fitted polynomial needs to be extrapolated. Other established methods, e.g., kriging methods (Strößenreuther et al., 2020), do not consider the elevation dependence. However, the elevation dependence could be included for kriging on mountain glaciers. The community would profit from dedicated research to study how voids add to the overall mass change uncertainty derived from CryoSat-2 data for, specifically, mountain glaciers.

The presented dataset is a swath-only dataset. We explicitly refrain from merging the additionally derived POCA data or from swath-processing the leading edge. There is no straightforward method to combine POCA and swath data. While it may seem odd to discard information, using them requires research on how the elevation estimates of the two datasets relate to each other. Note that the bias between POCA and swath data depends on the topography and the surface properties and will vary spatially and temporally. Further note, that POCA data should likely be weighted more than swath data because POCA data are based on multiple waveform samples. Successfully integrating POCA data could yield benefits around mountain tops and ice divides, especially. Elevation estimates from swath processing the leading edge are similarly biased with regard to the remainder of the waveform (Haacker et al., 2023). The associated received signal is reflected above the swath scattering horizon.

The product shows the expected fingerprint of surging glaciers in, e.g., Svalbard: gains at low elevations and losses at high elevations (Appendix A2, Fig. A4). Thus, CryoSwath is a promising tool to search for interesting study areas. The hypsometric change rate profiles could be used to automate finding potentially surging glaciers. With the versatile API, these profiles could easily be calculated using the `cryoswath.misc.interpolate_hypsometrically()` function and used for comparison on, e.g., a yearly basis.

7 Conclusions

In this work, we present the Python package CryoSwath 0.2.2, which allows deriving surface elevation data from ESA's CryoSat-2 SARIn L1b product at Baseline E. The workflow supports automated data filtering, resolving the phase ambiguity, locating the scatterer distributions, rasterizing the point elevation estimates, and interpolating any voids to arrive at monthly sampled, three-month rolling-window estimates on a 500 by 500 m grid. At the same time, users have a number of options to customize the processing within each step. CryoSwath provides means for researchers without prior SARIn swath processing knowledge to derive elevation change estimates for glacier surfaces. Being open-source, CryoSwath provides transparency and the ability to modify its implementation. While CryoSwath offers pipelines to immediately compute high-level products,

https://doi.org/10.5194/egusphere-2026-5522
Preprint. Discussion started: 27 October 2026
© Author(s) 2026. CC BY 4.0 License.

the intermediate results can be inspected at any time. CryoSwath optionally retains waveform diagnostics such as power and coherence in its point elevation outputs. Its modularity allows adding diagnostic output beyond the implemented options and, generally, replacing parts of the workflow according to custom demands. As MIT-licensed open-source software, CryoSwath can be adopted and advanced by the community.

The presented surface elevation data covers several first-order RGI regions: Alaska, Arctic Canada North and South, the Greenland Periphery, Iceland, Svalbard and Jan Mayen, Scandinavia, and the Russian Arctic. This dataset enables detailed analysis of the evolution and dynamics of individual glaciers, opening new avenues for follow-up research. Among the regions studied, glaciers in Alaska experienced the greatest ice loss, both in absolute and relative terms, with a mass loss of 80 ± 8 Gt yr^{-1} and a surface lowering of 1.10 ± 0.03 m yr^{-1}. Across all regions and subregions, surface elevation is decreasing. The smallest rates of surface lowering are observed in Arctic Canada North and the Greenland Periphery, with 0.27 ± 0.02 and 0.298 ± 0.015 m yr^{-1}, respectively. Within Iceland, the surface elevation of its ice caps shows localized increases, particularly over Vatnajökull, the country's largest ice cap. These elevation gains occur mainly at higher altitudes, while lower elevations continue to show significant losses. However, photogrammetric observations do not fully agree in the magnitude of these patterns, suggesting a possible discrepancy between changes in scattering-horizon elevation derived from CryoSat-2 data and changes in the actual surface elevation observed by photogrammetry. Investigating differences in elevation change rates between photogrammetry and radar altimetry may offer insights into firn densification processes (Otosaka et al., 2020). Moreover, the sign of the discrepancy between the two measurement techniques differs across regions. In Arctic Canada North and South, the Greenland Periphery, and Iceland, the photogrammetry-based mass balances are more negative, while in Svalbard and the Russian Arctic, CryoSat-2-derived trends are more negative. An Arctic-wide comparison of both methods could thus provide clues about regional climatological shifts.

Code and data availability. All code is published open-source under the MIT license, and all data are freely available under the CC-BY-4.0 license. The code for producing the datasets, CryoSwath, can be accessed at Zenodo under code DOI `10.5281/zenodo.14825358` (Haacker, 2025a), with the used version 0.2.2 specifically being available under DOI `10.5281/zenodo.15064780`. The remaining datasets and code are all archived in 4TU.ResearchData. The monthly elevation dataset is available under data DOI `10.4121/955d7f5a-0e3f-4166-a411-f0dcc4557cb2` (Haacker and Wouters, 2025b). The trend dataset is published under data DOI `10.4121/85738a14-6652-4e0c-8552-d6fc729141b3` (Haacker and Wouters, 2025a). The code that allows reproducing this manuscript including many of its figures and values can be accessed under code DOI `10.4121/fdad7bbe-0deb-43d4-9a41-237be0d60df6` (Haacker and Wouters, 2026b). Ancillary data that supports the reproduction code allowing skipping processing steps or validating products is accessible under data DOI `10.4121/48892e44-ec2a-434f-bac1-8b7e1507e7d2` (Haacker and Wouters, 2026a). The lists of glaciers that were grouped to divide the Greenland Periphery into subregions are archived under DOI `10.4121/fb61f7d2-6d70-4957-912f-e68fac846b56` (Haacker, 2025b).

https://doi.org/10.5194/egusphere-2026-5522
Preprint. Discussion started: 27 October 2026
© Author(s) 2026. CC BY 4.0 License.

Appendix A: Supplementary material

A1 Echo-coordinate derivation

The variables and reference frame are defined in Sect. 3.2 and illustrated in Fig. 2.

Below, we will calculate the echo origin location using the satellite position, its travel direction, the great-circle distance to the echo origin, and its elevation above the reference ellipsoid. The last two of the four are not yet known. With Eq. A1, we start off by calculating the length of $\boldsymbol{P}_{\text{scat}}$. We then compute the angle $\Delta\zeta$ between $\boldsymbol{P}_{\text{CS2}}$ and $\boldsymbol{P}_{\text{scat}}$ in Eq. A2. We continue in Eq. A3 (Torge and Müller, 2012, Ch. 4, Eq. 4.15) by calculating the Earth's radius of curvature r at nadir in the prime vertical plane. This is a good approximation because at the poles where the angle between CryoSat-2's across-track direction and the prime vertical plane is largest, the meridional radius of curvature approaches the radius of curvature in the prime vertical plane. Here, a and e refer to the WGS84 semi-major axis length and the eccentricity, respectively. Next, we calculate the elevation of the echo origin h in Eq. A4. Lastly, in Eq. A5, we approximate the ellipsoidal distance between nadir and the echo origin by the great-circle distance d_{off} with the curvature at nadir.

$$
\begin{aligned}
|\boldsymbol{P}_{\text{scat}}| &= \sqrt{(\boldsymbol{P}_{\text{CS2}} - (\boldsymbol{P}_{\text{CS2}} - \boldsymbol{P}_{\text{scat}}))^2} \\
&= \sqrt{|\boldsymbol{P}_{\text{CS2}}|^2 - 2 \cdot \cos(\theta)\, |\boldsymbol{P}_{\text{CS2}}|\, \overline{P_{\text{CS2}} P_{\text{scat}}} + \overline{P_{\text{CS2}} P_{\text{scat}}}^2}
\end{aligned} \tag{A1}
$$

$$
\Delta\zeta = \arctan\left(\frac{|\boldsymbol{P}_{\text{scat}}| \sin(\theta)}{|\boldsymbol{P}_{\text{CS2}}| - |\boldsymbol{P}_{\text{scat}}| \cos(\theta)} \right) \tag{A2}
$$

$$
r = \frac{a}{\sqrt{1 - e^2 \sin^2(\phi)}} \tag{A3}
$$

$$
h = |\boldsymbol{P}_{\text{scat}}| - r \tag{A4}
$$

$$
d_{\text{off}} = r \cdot \Delta\zeta \tag{A5}
$$

Now, having CryoSat-2's coordinates ϕ and λ, the direction to the echo origin $\alpha + 90°$, and the great-circle distance d_{off} between nadir and the echo origin, we use `pyproj` (Snow et al., 2025) to compute the echo-origin coordinates.

A2 Svalbard surge examples

Surface elevation trends for Svalbard are shown in Fig. A4. Multiple glaciers on Svalbard show thinning at higher elevations and thickening at the glacier fronts, indicating surge phases that, indeed, were reported earlier. Those are Wahlenbergbreen (Sevestre et al., 2018), Penckbreen and Sveitsarfonna (McCerery et al., 2024), Morsjnevbreen/Strongbreen (Kääb et al., 2023), and Recherchebreen (Kavan et al., 2024). Arnesenbreen (Kääb et al., 2023) shows the same signature, but less evident. On Austfonna, the most pronounced surge patterns are seen on Storisstraumen (also known as Basin-3) and the neighboring Basin-2 (Dunse et al., 2015; Morris et al., 2022).

https://doi.org/10.5194/egusphere-2026-5522
Preprint. Discussion started: 27 October 2026
© Author(s) 2026. CC BY 4.0 License.

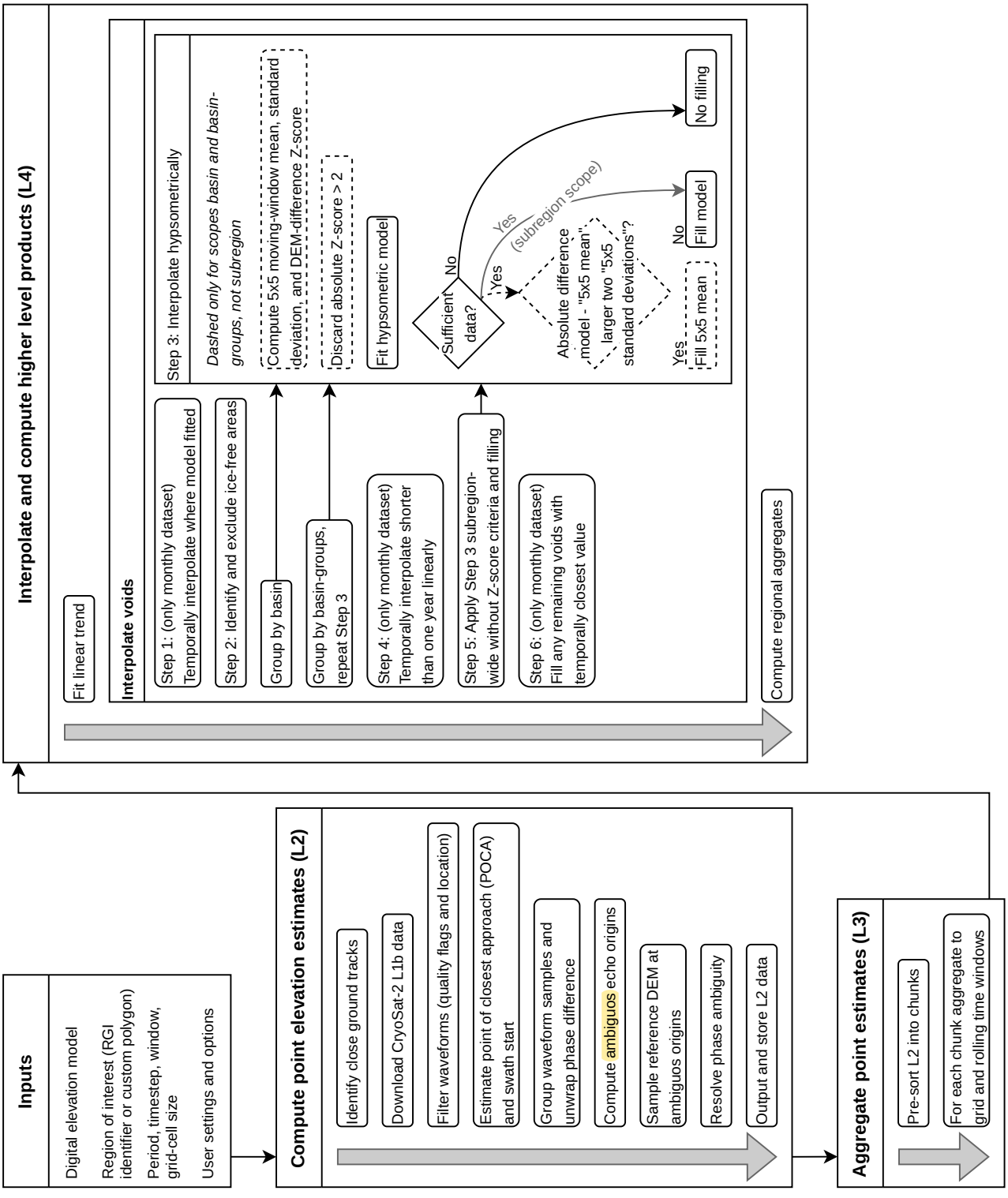

Figure A1. Flowchart of the algorithm to compute monthly rasterized surface elevation estimates and rasterized linear trends of the surface elevation. The items refer to the main text and should be understood in their context.

https://doi.org/10.5194/egusphere-2026-5522
Preprint. Discussion started: 27 October 2026
© Author(s) 2026. CC BY 4.0 License.

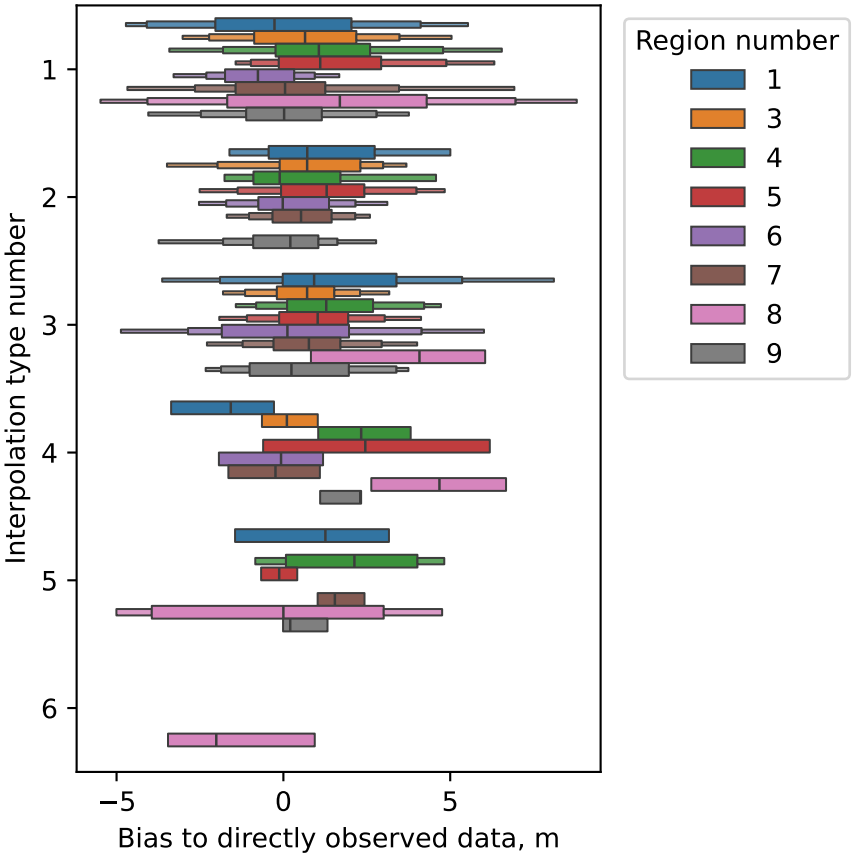

Figure A2. Boxenplot (Hofmann et al., 2017) of the bias by interpolation type and region with regard to directly observed data. See Sect. 4.3 for the calculation of the bias, which uses randomly chosen ArcticDEM strips. Interpolation type 1: a model using trend, annual, and semi-annual cycle components is fitted, 2: a hypsometric model is fitted per basin, 3: a hypsometric model is fitted across neighboring basins of the same termination type, 4: linear temporal interpolation for gaps shorter than one year, 5: hypsometric interpolation across second-order subregions, and 6: temporal nearest-neighbor filling. Region number 1: Alaska, 3: Arctic Canada North, 4: Arctic Canada South, 5: Greenland Periphery, 6: Iceland, 7: Svalbard, 8: Scandinavia, and 9: Russian Arctic.

https://doi.org/10.5194/egusphere-2026-5522
Preprint. Discussion started: 27 October 2026
© Author(s) 2026. CC BY 4.0 License.

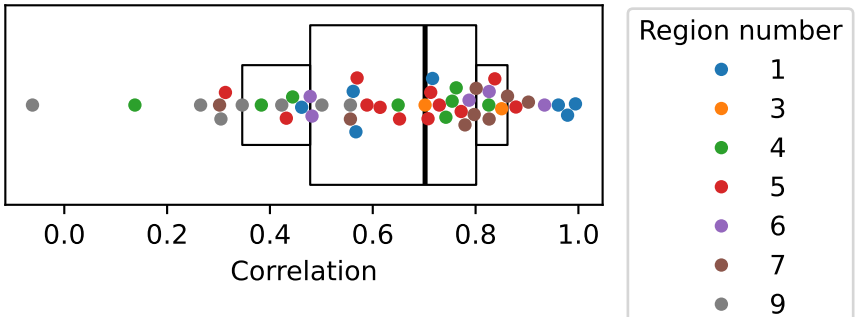

Figure A3. Boxen and swarm plots of temporal error correlations for measurements separated by one year. The errors are measured as deviation from ArcticDEM strip data. Region number 1: Alaska, 3: Arctic Canada North, 4: Arctic Canada South, 5: Greenland Periphery, 6: Iceland, 7: Svalbard, and 9: Russian Arctic. Scandinavia did not contribute applicable data to this analysis.

https://doi.org/10.5194/egusphere-2026-5522
Preprint. Discussion started: 27 October 2026
© Author(s) 2026. CC BY 4.0 License.

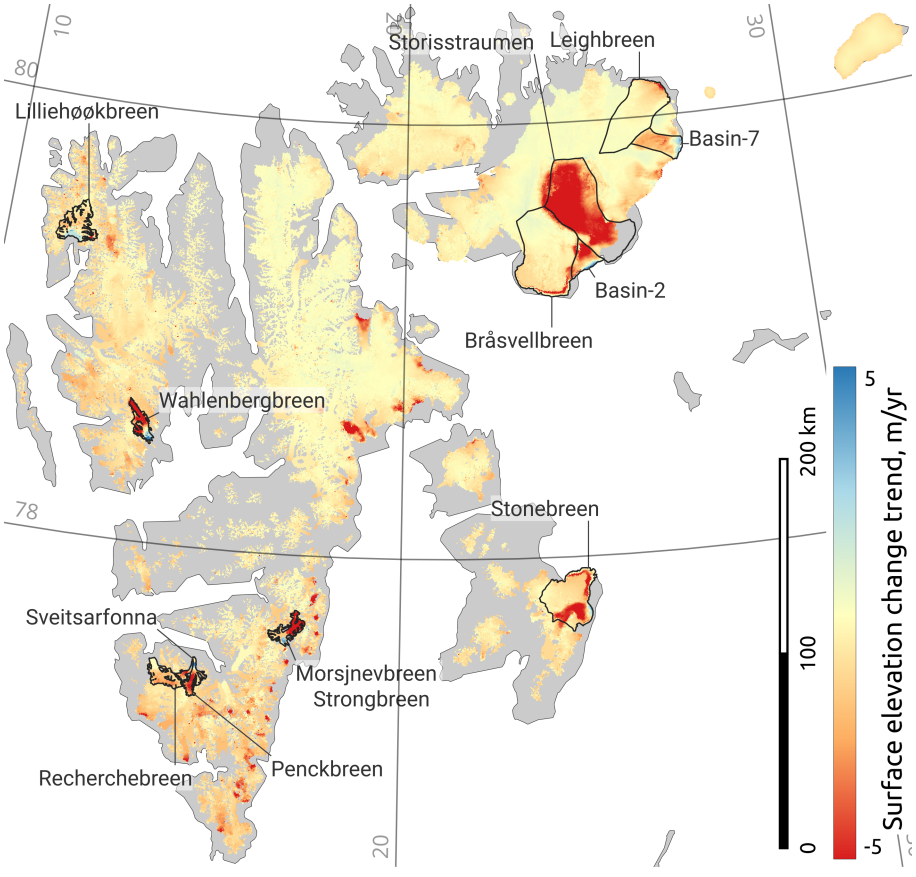

Figure A4. Surface elevation change rate of glaciers in Svalbard, 2010 – 2024. Selected surge examples are discussed in Appendix A2.

https://doi.org/10.5194/egusphere-2026-5522
Preprint. Discussion started: 27 October 2026
© Author(s) 2026. CC BY 4.0 License.

Table A1. List of measurement confidence data flags which were used to filter CryoSat-2 L1b input data, and their meanings (Scagliola and Geminale, 2020; Brockley, 2021).

Flag name	Flag meaning
`block_degraded`	Block Degraded. Set if the block is degraded and should not be processed.
`blank_block`	Blank Block. Set if a blank block has been inserted for record padding.
`datation_degraded`	Datation Degraded. Set if the datation is degraded.
`orbit_prop_error`	Orbit Propagation Error. Set if an error has been returned by a retracker algorithm or independent check.
`echo_saturated`	Echo Saturation. From the echo saturation flag from the telemetry.
`echo_rx1_error`	Receive Chain 1 (Rx1) Error. Set if the Rx1 chain raw echo is degraded or missing.
`echo_rx2_error`	Receive Chain 2 (Rx2) Error. Set if the Rx2 chain raw echo is degraded or missing.
`trk_echo_error`	Tracking Echo Error. Set if the tracking echo is degraded.
`other_echo_error`	Other Echo Error. Redundant: Set if one of `echo_rx1_error`, `echo_rx2_error`, or `trk_echo_error` are flagged.
`sarin_rx1_error`	SARIn Receive Chain 1 (Rx1) Error. Set if the Rx1 chain is degraded or missing.
`sarin_rx2_error`	SARIn Receive Chain 2 (Rx2) Error. Set if the Rx2 chain is degraded or missing.
`window_delay_error`	Window Delay Error. Set if the window delay value is out of range or if there is a computation error.
`agc_error`	Automatic gain control (AGC) Error. Set if the AGC value is out of range or if there is a computation error.
`npm_error`	Noise Power Measurement Error. Set if the NPM is degraded, out of range, or there is a computation error.
`power_scale_error`	Power Scaling Error. Set if there is an error in the power scaling of the echo (L1B waveform is null).

https://doi.org/10.5194/egusphere-2026-5522
Preprint. Discussion started: 27 October 2026
© Author(s) 2026. CC BY 4.0 License.

Table A2. Subregion overview. The table provides identifiers, subregion names, EPSG registry coordinate reference system identifiers, the covered area, the glacier area according to the Randolph Glacier Inventory (RGI) 7.0 (RGI 7.0 Consortium, 2023), and the area uncertainties u_{A1} and u_{A2} in the columns from left to right. The areas and their uncertainties are given in square kilometer. The identifiers are the same as the second-order region codes in the RGI, except for Greenland Periphery that has been split up into five custom subregions (see main text). Scandinavia is treated as a whole without considering each RGI second-order region separately.

ID	Name	EPSG	Covered area	RGI area	u_{A1}	u_{A2}
01-02	Alaska Range (Wrangell/Kilbuck)	32606	16286	16284	3	790
01-04	West Chugach Mountains (Talkeetna)	32606	11996	12005	9	559
01-05	Saint Elias Mountains	32607	32869	33178	309	912
01-06	North Coast Ranges	32608	22446	22964	518	1300
03-01	North Ellesmere Island	3413	26304	27690	1386	888
03-02	Axel Heiberg and Meighen Is	3413	11334	11852	518	382
03-03	North Central Ellesmere Island	3413	20354	21336	982	555
03-04	South Central Ellesmere Island	3413	18563	19322	759	400
03-05	South Ellesmere Island (Northwest Devon)	3413	9705	10042	337	339
03-06	Devon Island	3413	14590	15000	410	271
03-07	Melville Island	3413	122	128	6	5
04-01	Bylot Island	32617	4886	4883	3	159
04-02	West Baffin Island	32618	3757	3767	10	74
04-03	North Baffin Island	32617	504	497	7	39
04-04	Northeast Baffin Island	32618	8188	8195	8	423
04-05	East Central Baffin Island	32619	9420	9431	11	452
04-06	South East Baffin Island	32620	7589	7603	14	417
04-07	Cumberland Sound	32620	5894	5907	13	258
04-08	Frobisher Bay	32619	237	235	1	15
05-11	North Greenland	3413	34503	36331	1828	1223
05-12	West Greenland	32620	9979	9948	31	536
05-13	South West Greenland	32622	6662	6670	8	277
05-14	South East Greenland	32623	6533	6541	7	385
05-15	East Greenland	32626	30995	30993	2	1707
06-01	Iceland	32628	10841	11060	218	274
07-01	Svalbard	3413	32327	33841	1514	1028
08-01	North Scandinavia	32633	1419	1430	11	138
08-02	Southwest Scandinavia	32633	1220	1216	5	104
08-03	Southeast Scandinavia	32633	298	302	5	30
09-01	Franz Josef Land	3413	12112	12762	650	437
09-02	Novaya Zemlya	3413	21403	22132	729	536
09-03	Severnaya Zemlya	3413	15900	16701	801	396

https://doi.org/10.5194/egusphere-2026-5522
Preprint. Discussion started: 27 October 2026
© Author(s) 2026. CC BY 4.0 License.

Author contributions. BW and JH conceptualized the study. JH drafted the processing protocol. BW and JH revised the processing protocol. JH produced the datasets. BW and JH wrote the manuscript.

Competing interests. The authors declare that they have no conflict of interest.

Acknowledgements. We thank D.C. Slobbe for helpful comments that materially improved the manuscript. This study was supported by the Dutch Research Council (NWO) through VIDI grant 016.Vidi.171.063 and by the European Union's Horizon 2020 Programme through the PROTECT project, grant agreement No. 869304. The CryoSat-2 L1b product was provided by the European Space Agency (ESA), DEMs by the Polar Geospatial Center under NSF-OPP awards 1043681, 1559691, 1542736, 1810976, and 2129685, and glacier and glacier-complex outlines and ancillary data by the RGI 7.0 Consortium.

https://doi.org/10.5194/egusphere-2026-5522
Preprint. Discussion started: 27 October 2026
© Author(s) 2026. CC BY 4.0 License.

References

Berthier, E., Floricioiu, D., Gardner, A. S., Gourmelen, N., Jakob, L., Paul, F., Treichler, D., Wouters, B., Belart, J. M. C., Dehecq, A., Dussaillant, I., Hugonnet, R., Kääb, A., Krieger, L., Pálsson, F., and Zemp, M.: Measuring glacier mass changes from space—a review, Reports on Progress in Physics, 86, 036 801, https://doi.org/10.1088/1361-6633/acaf8e, 2023.

Brockley, D.: CryoSat Ice netCDF L2 Product Format Specification [PFS-I-L2], Product Format Specification C2-RS-ACS-ESL-5265, Advanced Computer Systems, https://earth.esa.int/eogateway/documents/20142/37627/CryoSat-netCDF-L2-Product-Format-Specification.pdf, 2021.

Ciracì, E., Velicogna, I., and Swenson, S.: Continuity of the Mass Loss of the World's Glaciers and Ice Caps From the GRACE and GRACE Follow-On Missions, Geophysical Research Letters, 47, e2019GL086 926, https://doi.org/10.1029/2019GL086926, 2020.

CryoTEMPO-EOLIS: CryoTEMPO-EOLIS product handbook, Tech. Rep. CS_CTS_PHB_EWAVE_0401, European Space Agency, https://cryotempo-eolis.org/wp-content/uploads/sites/4/2022/08/CryoTempo-ThematicProduct-ProductHandbook_Latest.pdf, 2026.

Drinkwater, M. R., Francis, R., Ratier, G., and Wingham, D. J.: The European Space Agency's Earth Explorer Mission CryoSat: measuring variability in the cryosphere, Annals of Glaciology, 39, 313–320, https://doi.org/10.3189/172756404781814663, 2004.

Dunse, T., Schellenberger, T., Hagen, J. O., Kääb, A., Schuler, T. V., and Reijmer, C. H.: Glacier-surge mechanisms promoted by a hydro-thermodynamic feedback to summer melt, The Cryosphere, 9, 197–215, https://doi.org/10.5194/tc-9-197-2015, 2015.

Dussaillant, I., Hugonnet, R., Huss, M., Berthier, E., Bannwart, J., Paul, F., and Zemp, M.: Annual mass change of the world's glaciers from 1976 to 2024 by temporal downscaling of satellite data with in situ observations, Earth System Science Data, 17, 1977–2006, https://doi.org/10.5194/essd-17-1977-2025, 2025.

Eaton, B., Gregory, J., Drach, B., Taylor, K., Hankin, S., Caron, J., Signell, R., Bentley, P., Rappa, G., Höck, H., Pamment, A., Juckes, M., Raspaud, M., Blower, J., Horne, R., Whiteaker, T., Blodgett, D., Zender, C., Lee, D., Hassell, D., Snow, A. D., Kölling, T., Allured, D., Jelenak, A., Soerensen, A. M., Gaultier, L., Herlédan, S., Manzano, F., Bärring, L., Barker, C., and Bartholomew, S. L.: NetCDF Climate and Forecast (CF) Metadata Conventions, https://doi.org/10.5281/ZENODO.14275599, 2024.

European Space Agency: L1b SARin Precise Orbit, https://doi.org/10.5270/cr2-6afef01, 2019.

European Space Agency: New CryoSat Geographical Mode Mask v5.0 now in operation - Earth Online, https://earth.esa.int/eogateway/news/new-cryosat-geographical-mode-mask-v5-0-now-in-operation, 2023.

Foresta, L., Gourmelen, N., Pálsson, F., Nienow, P., Björnsson, H., and Shepherd, A.: Surface elevation change and mass balance of Icelandic ice caps derived from swath mode CryoSat-2 altimetry, Geophysical Research Letters, 43, 12,138–12,145, https://doi.org/10.1002/2016GL071485, 2016.

Foresta, L., Gourmelen, N., Weissgerber, F., Nienow, P., Williams, J. J., Shepherd, A., Drinkwater, M. R., and Plummer, S.: Heterogeneous and rapid ice loss over the Patagonian Ice Fields revealed by CryoSat-2 swath radar altimetry, Remote Sensing of Environment, 211, 441–455, https://doi.org/10.1016/j.rse.2018.03.041, 2018.

Garcia-Mondéjar, A., Gourmelen, N., Escorihuela, M. J., Roca, M., Shepherd, A., and Plummer, S.: Multisurface Retracker for Swath Processing of Interferometric Radar Altimetry, IEEE Geoscience and Remote Sensing Letters, 16, 1839–1843, https://doi.org/10.1109/LGRS.2019.2913635, 2019.

Gardner, A. S., Moholdt, G., Cogley, J. G., Wouters, B., Arendt, A. A., Wahr, J., Berthier, E., Hock, R., Pfeffer, W. T., Kaser, G., Ligtenberg, S. R. M., Bolch, T., Sharp, M. J., Hagen, J. O., van den Broeke, M. R., and Paul, F.: A Reconciled Estimate of Glacier Contributions to Sea Level Rise: 2003 to 2009, Science, 340, 852–857, https://doi.org/10.1126/science.1234532, 2013.

https://doi.org/10.5194/egusphere-2026-5522
Preprint. Discussion started: 27 October 2026
© Author(s) 2026. CC BY 4.0 License.

Gourmelen, N., Escorihuela, M. J., Shepherd, A., Foresta, L., Muir, A., Garcia-Mondéjar, A., Roca, M., Baker, S. G., and Drinkwater, M. R.: CryoSat-2 swath interferometric altimetry for mapping ice elevation and elevation change, Advances in Space Research, 62, 1226–1242, https://doi.org/10.1016/j.asr.2017.11.014, 2018.

Gray, L., Burgess, D., Copland, L., Cullen, R., Galin, N., Hawley, R., and Helm, V.: Interferometric swath processing of Cryosat data for glacial ice topography, The Cryosphere, 7, 1857–1867, https://doi.org/10.5194/tc-7-1857-2013, 2013.

Gray, L., Burgess, D., Copland, L., Langley, K., Gogineni, P., Paden, J., Leuschen, C., van As, D., Fausto, R., Joughin, I., and Smith, B.: Measuring Height Change Around the Periphery of the Greenland Ice Sheet With Radar Altimetry, Frontiers in Earth Science, 7, 146, https://doi.org/10.3389/feart.2019.00146, 2019.

Haacker, J.: CryoSwath: CryoSat-2 swath processing package, Zenodo, https://doi.org/10.5281/zenodo.14825358, 2025a.

Haacker, J.: Lists of glacier and complex IDs accompanying the article "CryoSwath: a CryoSat-2 swath processor and monthly surface elevation dataset for Arctic mountain glaciers", https://doi.org/10.4121/FB61F7D2-6D70-4957-912F-E68FAC846B56, 2025b.

Haacker, J. and Wouters, B.: Glacier surface elevation change rate dataset accompanying the article "CryoSwath: a CryoSat-2 swath processor and monthly surface elevation dataset for Arctic mountain glaciers", https://doi.org/10.4121/85738A14-6652-4E0C-8552-D6FC729141B3, 2025a.

Haacker, J. and Wouters, B.: Glacier surface elevation dataset accompanying the article "CryoSwath: a CryoSat-2 swath processor and monthly surface elevation dataset for Arctic mountain glaciers", https://doi.org/10.4121/955D7F5A-0E3F-4166-A411-F0DCC4557CB2, 2025b.

Haacker, J. and Wouters, B.: Ancilliary data for the reproduction workflow of the article "CryoSwath: a CryoSat-2 swath processor and monthly surface elevation dataset for Arctic mountain glaciers", https://doi.org/10.4121/48892E44-EC2A-434F-BAC1-8B7E1507E7D2, 2026a.

Haacker, J. and Wouters, B.: Workflow for the reproduction of the article "CryoSwath: a CryoSat-2 swath processor and monthly surface elevation dataset for Arctic mountain glaciers", 4TU.ResearchData, https://doi.org/10.4121/FDAD7BBE-0DEB-43D4-9A41-237BE0D60DF6, 2026b.

Haacker, J., Wouters, B., and Slobbe, C.: Systematic errors observed in CryoSat-2 elevation swaths on mountain glaciers and their implications, IEEE Transactions on Geoscience and Remote Sensing, 61, 1–12, https://doi.org/10.1109/TGRS.2023.3277277, 2023.

Hawley, R. L., Shepherd, A., Cullen, R., Helm, V., and Wingham, D. J.: Ice-sheet elevations from across-track processing of airborne interferometric radar altimetry, Geophysical Research Letters, 36, 2009GL040 416, https://doi.org/10.1029/2009GL040416, 2009.

Hofmann, H., Wickham, H., and Kafadar, K.: Letter-Value Plots: Boxplots for Large Data, Journal of Computational and Graphical Statistics, 26, 469–477, https://doi.org/10.1080/10618600.2017.1305277, 2017.

Höhle, J. and Höhle, M.: Accuracy assessment of digital elevation models by means of robust statistical methods, ISPRS Journal of Photogrammetry and Remote Sensing, 64, 398–406, https://doi.org/10.1016/j.isprsjprs.2009.02.003, 2009.

Hugonnet, R., McNabb, R., Berthier, E., Menounos, B., Nuth, C., Girod, L., Farinotti, D., Huss, M., Dussaillant, I., Brun, F., and Kääb, A.: Accelerated global glacier mass loss in the early twenty-first century, Nature, 592, 726–731, https://doi.org/10.1038/s41586-021-03436-z, 2021.

Huss, M.: Density assumptions for converting geodetic glacier volume change to mass change, The Cryosphere, 7, 877–887, https://doi.org/10.5194/tc-7-877-2013, 2013.

Jakob, L. and Gourmelen, N.: Glacier mass loss between 2010 and 2020 dominated by atmospheric forcing, Geophysical Research Letters, 50, e2023GL102 954, https://doi.org/10.1029/2023GL102954, 2023.

https://doi.org/10.5194/egusphere-2026-5522
Preprint. Discussion started: 27 October 2026
© Author(s) 2026. CC BY 4.0 License.

Jakob, L., Gourmelen, N., Ewart, M., and Plummer, S.: Spatially and temporally resolved ice loss in High Mountain Asia and the Gulf of Alaska observed by CryoSat-2 swath altimetry between 2010 and 2019, The Cryosphere, 15, 1845–1862, https://doi.org/10.5194/tc-15-1845-2021, 2021.

Johnson, D. H. and Dudgeon, D. E.: Array signal processing: concepts and techniques, Prentice-Hall signal processing series, P T R Prentice Hall, Englewood Cliffs, NJ, ISBN 0-13-048513-6 978-0-13-048513-7, https://www.informit.com/store/array-signal-processing-concepts-and-techniques-9780130485137, 1993.

Kääb, A., Bazilova, V., Leclercq, P. W., Mannerfelt, E. S., and Strozzi, T.: Global clustering of recent glacier surges from radar backscatter data, 2017–2022, Journal of Glaciology, 69, 1515–1523, https://doi.org/10.1017/jog.2023.35, 2023.

Kavan, J., Strzelecki, M. C., Benn, D. I., Luckman, A., Roman, M., and Zagórski, P.: Glacier surge as a trigger for the fastest delta growth in the Arctic, Communications Earth & Environment, 5, https://doi.org/10.1038/s43247-024-01877-8, 2024.

McCerery, R., Davies, B. J., Lovell, H., Pearce, D. A., Calvo-Ryan, R., Małecki, J., and Woodward, J.: Terrestrial glacial geomorphology of surge-type and non-surge-type glaciers on Svalbard, Journal of Maps, 20, 2362 277, https://doi.org/10.1080/17445647.2024.2362277, 2024.

McNabb, R., Nuth, C., Kääb, A., and Girod, L.: Sensitivity of glacier volume change estimation to DEM void interpolation, The Cryosphere, 13, 895–910, https://doi.org/10.5194/tc-13-895-2019, 2019.

Morris, A., Moholdt, G., and Gray, L.: Spread of Svalbard Glacier Mass Loss to Barents Sea Margins Revealed by CryoSat-2, Journal of Geophysical Research: Earth Surface, 125, e2019JF005 357, https://doi.org/10.1029/2019JF005357, 2020.

Morris, A., Moholdt, G., Gray, L., Schuler, T. V., and Eiken, T.: CryoSat-2 interferometric mode calibration and validation: A case study from the Austfonna ice cap, Svalbard, Remote Sensing of Environment, 269, 112 805, https://doi.org/10.1016/j.rse.2021.112805, 2022.

Otosaka, I. N., Shepherd, A., Casal, T. G. D., Coccia, A., Davidson, M., Bella, A. D., Fettweis, X., Forsberg, R., Helm, V., Hogg, A. E., Hvidegaard, S. M., Lemos, A., Macedo, K., Munneke, P. K., Parrinello, T., Simonsen, S. B., Skourup, H., and Sørensen, L. S.: Surface Melting Drives Fluctuations in Airborne Radar Penetration in West Central Greenland, Geophysical Research Letters, 47, e2020GL088 293, https://doi.org/10.1029/2020GL088293, 2020.

Pedregosa, F., Varoquaux, G., Gramfort, A., Michel, V., Thirion, B., Grisel, O., Blondel, M., Prettenhofer, P., Weiss, R., Dubourg, V., Vanderplas, J., Passos, A., Cournapeau, D., Brucher, M., Perrot, M., and Duchesnay, É.: Scikit-learn: Machine Learning in Python, Journal of Machine Learning Research, 12, 2825–2830, http://jmlr.org/papers/v12/pedregosa11a.html, 2011.

Pfeffer, W. T., Arendt, A. A., Bliss, A., Bolch, T., Cogley, J. G., Gardner, A. S., Hagen, J.-O., Hock, R., Kaser, G., Kienholz, C., Miles, E. S., Moholdt, G., Mölg, N., Paul, F., Radić, V., Rastner, P., Raup, B. H., Rich, J., Sharp, M. J., and The Randolph Consortium: The Randolph Glacier Inventory: a globally complete inventory of glaciers, Journal of Glaciology, 60, 537–552, https://doi.org/10.3189/2014JoG13J176, 2014.

Porter, C., Howat, I., Noh, M.-J., Husby, E., Khuvis, S., Danish, E., Tomko, K., Gardiner, J., Negrete, A., Yadav, B., Klassen, J., Kelleher, C., Cloutier, M., Bakker, J., Enos, J., Arnold, G., Bauer, G., and Morin, P.: ArcticDEM - Mosaics, Version 4.1, https://doi.org/10.7910/DVN/3VDC4W, 2023.

Raney, R.: The delay/Doppler radar altimeter, IEEE Transactions on Geoscience and Remote Sensing, 36, 1578–1588, https://doi.org/10.1109/36.718861, 1998.

RGI 7.0 Consortium: Randolph Glacier Inventory - A Dataset of Global Glacier Outlines, https://doi.org/10.5067/F6JMOVY5NAVZ, 2023.

https://doi.org/10.5194/egusphere-2026-5522
Preprint. Discussion started: 27 October 2026
© Author(s) 2026. CC BY 4.0 License.

Rounce, D. R., Hock, R., Maussion, F., Hugonnet, R., Kochtitzky, W., Huss, M., Berthier, E., Brinkerhoff, D., Compagno, L., Copland, L., Farinotti, D., Menounos, B., and McNabb, R. W.: Global glacier change in the 21st century: Every increase in temperature matters, Science, 379, 78–83, https://doi.org/10.1126/science.abo1324, 2023.

Scagliola, M. and Geminale, T.: CryoSat Ice netCDF L1B Product Format Specification [PFS-I-L1B], Product Format Specification C2-RS-ACS-ESL-5364, Advanced Computer Systems, https://earth.esa.int/eogateway/documents/20142/37627/CryoSat-netCDF-L1b-Product-Format-Specification.pdf, 2020.

scikit-learn developers: scikit-learn, Zenodo, https://doi.org/10.5281/ZENODO.591564, 2026.

Sevestre, H., Benn, D. I., Luckman, A., Nuth, C., Kohler, J., Lindbäck, K., and Pettersson, R.: Tidewater Glacier Surges Initiated at the Terminus, Journal of Geophysical Research: Earth Surface, 123, 1035–1051, https://doi.org/10.1029/2017JF004358, 2018.

Snow, A. D., Whitaker, J., Cochran, M., Miara, I., van den Bossche, J., Mayo, C., Lucas, G., Cochrane, P., de Kloe, J., Karney, C., Shaw, J. J., Anh, T. Q., Filipe, Ouzounoudis, G., Dearing, J., Lostis, G., Couwenberg, B., Hoese, D., de Bittencourt, H., Little, B., May, R., Itkin, M., McDonald, D., Schneck, C., Gohlke, C., Jurd, B., Raspaud, M., Brett, M., and Meulien, M.: pyproj4/pyproj: 3.7.1 Release, Zenodo, https://doi.org/10.5281/zenodo.14876934, 2025.

Strößenreuther, U., Horwath, M., and Schröder, L.: How Different Analysis and Interpolation Methods Affect the Accuracy of Ice Surface Elevation Changes Inferred from Satellite Altimetry, Mathematical Geosciences, 52, 499–525, https://doi.org/10.1007/s11004-019-09851-3, 2020.

The GlaMBIE Team, Zemp, M., Jakob, L., Dussaillant, I., Nussbaumer, S. U., Gourmelen, N., Dubber, S., A, G., Abdullahi, S., Andreassen, L. M., Berthier, E., Bhattacharya, A., Blazquez, A., Boehm Vock, L. F., Bolch, T., Box, J., Braun, M. H., Brun, F., Cicero, E., Colgan, W., Eckert, N., Farinotti, D., Florentine, C., Floricioiu, D., Gardner, A., Harig, C., Hassan, J., Hugonnet, R., Huss, M., Jóhannesson, T., Liang, C.-C. A., Ke, C.-Q., Khan, S. A., King, O., Kneib, M., Krieger, L., Maussion, F., Mattea, E., McNabb, R., Menounos, B., Miles, E., Moholdt, G., Nilsson, J., Pálsson, F., Pfeffer, J., Piermattei, L., Plummer, S., Richter, A., Sasgen, I., Schuster, L., Seehaus, T., Shen, X., Sommer, C., Sutterley, T., Treichler, D., Velicogna, I., Wouters, B., Zekollari, H., and Zheng, W.: Community estimate of global glacier mass changes from 2000 to 2023, Nature, 639, 382–388, https://doi.org/10.1038/s41586-024-08545-z, 2025.

Torge, W. and Müller, J.: Geodesy, De Gruyter, Berlin, Boston, ISBN 978-3-11-020718-7, https://doi.org/10.1515/9783110250008, 2012.

Wingham, D. J., Francis, C. R., Baker, S., Bouzinac, C., Brockley, D., Cullen, R., de Chateau-Thierry, P., Laxon, S. W., Mallow, U., Mavrocordatos, C., Phalippou, L., Ratier, G., Rey, L., Rostan, F., Viau, P., and Wallis, D. W.: CryoSat: A mission to determine the fluctuations in Earth's land and marine ice fields, Advances in Space Research, 37, 841–871, https://doi.org/10.1016/j.asr.2005.07.027, 2006.

Wolken, G. J., Wouters, B., Sharp, M., Andreassen, L. M., Baker, E. H., Burgess, D., Kohler, J., Luks, B., and O'Neel, S.: Glaciers and ice caps outside Greenland, in: State of the Climate in 2019, pp. S260–S265, Bulletin of the American Meteorological Society, https://doi.org/10.1175/BAMS-D-20-0086.1, 2020.

Wouters, B., Gardner, A. S., and Moholdt, G.: Global glacier mass loss during the GRACE satellite mission (2002-2016), Frontiers in Earth Science, 7, https://doi.org/10.3389/feart.2019.00096, 2019.